

# $K_{\ell 3}$ form factors at the physical point: Toward the continuum limit

Ken-ichi Ishikawa,<sup>1,2</sup> Naruhito Ishizuka,<sup>3</sup> Yoshinobu Kuramashi,<sup>3</sup> Yusuke Namekawa,<sup>4</sup>  
Yusuke Taniguchi,<sup>3</sup> Naoya Ukita,<sup>3</sup> Takeshi Yamazaki,<sup>5,3</sup> and Tomoteru Yoshié<sup>3</sup>

(PACS Collaboration)

<sup>1</sup>*Graduate School of Advanced Science and Engineering,  
Hiroshima University, Higashi-Hiroshima, Hiroshima 739-8526, Japan*

<sup>2</sup>*Core of Research for the Energetic Universe,  
Graduate School of Advanced Science and Engineering,  
Hiroshima University, Higashi-Hiroshima, Hiroshima 739-8526, Japan*

<sup>3</sup>*Center for Computational Sciences, University of Tsukuba,  
Tsukuba, Ibaraki 305-8577, Japan*

<sup>4</sup>*Department of Physics, Kyoto University,  
Kitashirakawa-Oiwake-cho, Kyoto 606-8502, Japan*

<sup>5</sup>*Faculty of Pure and Applied Sciences, University of Tsukuba,  
Tsukuba, Ibaraki 305-8571, Japan*

(Dated: October 6 2022)

## Abstract

We present updated results for the form factors of the kaon semileptonic ( $K_{\ell 3}$ ) decay process calculated with  $N_f = 2 + 1$  nonperturbatively  $O(a)$ -improved Wilson quark action and Iwasaki gauge action at the physical point on large volumes of more than  $(10 \text{ fm})^4$ . In addition to our previous calculation at the lattice spacing  $a = 0.085 \text{ fm}$ , we perform a calculation at the second lattice spacing of  $0.063 \text{ fm}$ . Using the results for the form factors extracted from 3-point functions with the local and also conserved vector currents at the two lattice spacings, continuum extrapolation and interpolation of the momentum transfer are carried out simultaneously to obtain the value of the form factor  $f_+(0)$  at the zero momentum transfer in the continuum limit. After investigation of stability of  $f_+(0)$  against several fit forms and different data, we obtain  $f_+(0) = 0.9615(10)(^{+47}_{-3})(5)$ , where the first, second, and third errors are statistical, systematic errors from choice of the fit forms and isospin breaking effect, respectively. Furthermore, we obtain the slope and curvature of the form factors, and the phase space integral from the momentum transfer dependence of the form factors. Combining our value of  $f_+(0)$  and experimental input of the  $K_{\ell 3}$  decay, one of the Cabibbo-Kobayashi-Maskawa matrix elements  $|V_{us}|$  is determined as  $|V_{us}| = 0.2252(_{-12}^{+5})$ , whose error contains the experimental one as well as that in the lattice calculation. This value is reasonably consistent with the ones determined from recent lattice QCD results of  $f_+(0)$  and also the one determined through the kaon leptonic decay process. We observe some tension between our value and  $|V_{us}|$  evaluated from the unitarity of the CKM matrix with  $|V_{ud}|$ , while it depends on the size of the error of  $|V_{ud}|$ . It is also found that  $|V_{us}|$  determined with our phase space integrals through six  $K_{\ell 3}$  decay processes is consistent with the above one using  $f_+(0)$ .

## I. INTRODUCTION

Unitarity of the Cabibbo-Kobayashi-Maskawa (CKM) matrix is important in search for signals beyond the standard model (BSM). Since it should be satisfied in the standard model, its violation indirectly suggests existence of a BSM physics. The unitarity of the first row of the CKM matrix gives a condition for the three matrix elements,  $|V_{ud}|$ ,  $|V_{us}|$ , and  $|V_{ub}|$ , as  $|V_{ud}|^2 + |V_{us}|^2 + |V_{ub}|^2 = 1$ . In the current values of the matrix elements reviewed in PDG20 [1],  $|V_{ud}| = 0.97370(14)$ ,  $|V_{us}| = 0.2245(8)$ , and  $|V_{ub}| = 0.00382(24)$ , the tension of  $3.3 \sigma$  from unity is observed as

$$1 - (|V_{ud}|^2 + |V_{us}|^2 + |V_{ub}|^2) = 0.00149(45). \quad (1)$$

It could be a BSM signal, though the value of  $|V_{us}|$  is obtained from an average of slightly different values,  $|V_{us}| = 0.2252(5)$  and  $0.2231(7)$  determined from the kaon leptonic ( $K_{\ell 2}$ ) and semileptonic ( $K_{\ell 3}$ ) decay processes, respectively. The error reductions, especially in the  $K_{\ell 3}$  decay, are desirable to clarify the tension. In both the determinations, lattice QCD calculation plays an essential role.

For the  $K_{\ell 2}$  decay,  $|V_{us}|$  is determined by combining the experimental values  $|V_{us}|F_K/|V_{ud}|F_\pi = 0.27599(37)$  [2] and  $|V_{ud}|$ , and the lattice QCD result of the ratio of the decay constants for the kaon and pion,  $F_K/F_\pi$ . In lattice QCD, its calculation is relatively simpler, and it is well determined in various calculations as reviewed in Ref. [3].

In the  $K_{\ell 3}$  decay,  $|V_{us}|$  is related to the kaon decay rate  $\Gamma_{K_{\ell 3}}$  as

$$\Gamma_{K_{\ell 3}} = C_{K_{\ell 3}}(|V_{us}|f_+(0))^2 I_K^\ell, \quad (2)$$

where  $f_+(0)$  is the value of the  $K_{\ell 3}$  form factor at  $q^2 = 0$  with  $q$  being the momentum transfer,  $C_{K_{\ell 3}}$  is a known factor including the electromagnetic correction and the SU(2) breaking effect.  $I_K^\ell$  is the phase space integral for  $\ell = e, \mu$ , which is calculated from the shape of the experimental  $K_{\ell 3}$  form factors. The value of  $f_+(0)$  is needed to be computed in a nonperturbative QCD calculation, such as lattice QCD. In lattice QCD, the calculation of  $f_+(0)$  is not as simple as the one of  $F_K/F_\pi$ , although several lattice QCD calculations [4–11] provided precise results of  $f_+(0)$ . The recent results of  $f_+(0)$  tend to yield a smaller  $|V_{us}|$  than the ones determined from the  $K_{\ell 2}$  decay and also the unitarity of the CKM matrix.

For the BSM search, it is important to confirm the discrepancies of  $|V_{us}|$  from several calculations by different groups using independent setups with a similar size of error to

the most precise result [11]. For this purpose we calculated the  $K_{\ell 3}$  form factors using a part of the PACS10 configurations [12]. The PACS10 configurations were generated on the physical volume of more than  $(10 \text{ fm})^4$  at the physical point, where the pion mass  $m_\pi$  and kaon mass  $m_K$  are the physical ones. This ensemble is suitable for a precise calculation of  $f_+(0)$ , because systematic errors for the chiral extrapolation and the finite volume effect are considered to be negligible. Furthermore, the data of the  $K_{\ell 3}$  form factors near  $q^2 = 0$  can be calculated even in the periodic boundary condition in the spatial directions thanks to the huge volume, so that a stable  $q^2$  interpolation of the  $K_{\ell 3}$  form factors is performed. In our previous calculation the obtained value of  $|V_{us}|$  with  $f_+(0)$  was consistent with the one from the  $K_{\ell 2}$  decay, while our error was larger than the one in Ref. [11]. Since our calculation was carried out at one lattice spacing,  $a = 0.085 \text{ fm}$ , the largest uncertainty of  $f_+(0)$  comes from a systematic error of a finite lattice spacing effect. Thus, the purpose of this study is to reduce the large systematic uncertainty by adding data calculated with another set of the PACS10 configurations at the finer lattice spacing,  $a = 0.063 \text{ fm}$ . We also aim to perform continuum extrapolation and  $q^2$  interpolation simultaneously to estimate the value of  $f_+(0)$  in the continuum limit using the form factors at the two lattice spacings.

In this calculation, not only local but also conserved vector currents are employed in the calculation of 3-point functions, from which the matrix elements of the  $K_{\ell 3}$  form factors are extracted. We newly calculate the conserved vector current data at  $a = 0.085 \text{ fm}$ , because in our previous calculation only the local vector current is employed at this lattice spacing. The results of  $f_+(0)$  obtained from the two currents have a different dependence on the lattice spacing. It enables us to carry out a continuum extrapolation of  $f_+(0)$  using only the two lattice spacings. The extrapolated result of  $f_+(0)$  in the continuum limit agrees with the one in our previous work, and also it has much smaller statistical and lower systematic errors than the previous one. The upper systematic error, however, is still a similar size to that in the previous work, which is mainly caused by a fit form dependence in the continuum extrapolation. This result reasonably agrees with the previous lattice QCD results within  $1.6 \sigma$  in the total error, where the statistical and systematic errors are added in quadrature. As in the previous work,  $|V_{us}|$  determined from our  $f_+(0)$  is well consistent with the one from the  $K_{\ell 2}$  decay. A tension is seen in a comparison of our value of  $|V_{us}|$  with the one evaluated from the unitarity of the CKM matrix, while its significance depends on the size of the error of  $|V_{ud}|$ . The slope and curvature of the form factors are also evaluated from

the continuum limit results for the form factors. Although the systematic errors coming from a fit function dependence are large in those results, except for the slope of  $f_+(q^2)$ , the results are reasonably consistent with the experimental ones and also the previous lattice QCD calculations. Furthermore, it is found that the phase space integrals calculated from our result of the  $q^2$  dependent form factors agree with the experimental values. Moreover, the values of  $|V_{us}|$  are determined from our phase space integrals through six kaon decay processes and their average. Those results also agree with that using  $f_+(0)$ . A part of the preliminary results in this work was already reported in Ref. [13].

This paper is organized as follows. Section II describes the definition of the  $K_{\ell 3}$  form factors, simulation parameters, and our calculation methods to extract the matrix elements. The results of the form factors using the local and conserved currents are presented in Sec. III including their  $q^2$  interpolations to  $q^2 = 0$  at each lattice spacing. Continuum extrapolations of the form factors are discussed in Sec. IV, where the results for  $f_+(0)$ , their slope and curvature, the phase space integrals, and determination of  $|V_{us}|$  are also presented. Section V is devoted to conclusion. The appendix summarizes various fit results of continuum extrapolations.

All dimensionful quantities are expressed in units of the lattice spacing throughout this paper, unless otherwise explicitly specified.

## II. CALCULATION METHODS

We calculate the two form factors of the  $K_{\ell 3}$  decay  $f_+(q^2)$  and  $f_0(q^2)$  defined below. In this section we first give the definitions of the form factors from the matrix element. After that, the simulation parameters, calculation method for the correlators, and analysis method to extract the matrix elements from the correlators are described.

### A. Definition of $K_{\ell 3}$ form factors

The  $K_{\ell 3}$  form factors  $f_+(q^2)$  and  $f_-(q^2)$  are defined by the matrix element of the weak vector current  $V_\mu$  as,

$$\langle \pi(\vec{p}_\pi) | V_\mu | K(\vec{p}_K) \rangle = (p_K + p_\pi)_\mu f_+(q^2) + (p_K - p_\pi)_\mu f_-(q^2), \quad (3)$$

where  $q = p_K - p_\pi$  is the four-dimensional momentum transfer. The scalar form factor  $f_0(q^2)$  is defined by  $f_+(q^2)$  and  $f_-(q^2)$  as,

$$f_0(q^2) = f_+(q^2) + \frac{-q^2}{m_K^2 - m_\pi^2} f_-(q^2) = f_+(q^2) \left( 1 + \frac{-q^2}{m_K^2 - m_\pi^2} \xi(q^2) \right), \quad (4)$$

where  $\xi(q^2) = f_-(q^2)/f_+(q^2)$ . At  $q^2 = 0$ , the two form factors  $f_+(q^2)$  and  $f_0(q^2)$  satisfy the condition  $f_+(0) = f_0(0)$ .

## B. Simulation parameters and setup

We employ a subset of the PACS10 configurations at the two bare couplings  $\beta = 2.00$  and 1.82, which are generated at the physical point on more than  $(10 \text{ fm})^4$  volume. The lattice size and lattice cutoff determined from the  $\Xi$  baryon mass input are tabulated in Table I. The configuration generations were performed using the nonperturbatively improved Wilson quark action with the six-stout link smearing [14] and the Iwasaki gauge action [15]. The simulation parameters of the configuration generation at  $\beta = 2.00$  and  $\beta = 1.82$  are summarized in Refs. [16] and [17], respectively. The number of the configuration used in this calculation is 20 at both the lattice spacings. The separations between each configuration are 5 and 10 molecular dynamics trajectories at  $\beta = 2.00$  and 1.82, respectively.

The same quark action as in the configuration generation is adopted in the measurement of the  $K_{\ell 3}$  form factors. The parameters for the quark actions are summarized in Table II. The parameters at  $\beta = 1.82$  are also found in our previous paper [12]. The coefficient of the clover term is nonperturbatively determined in the Schrödinger functional scheme. The stout smearing parameter is  $\rho = 0.1$  at both the lattice spacings. The statistical error of observables is evaluated by the jackknife method with the bin size of 5 and 10 trajectories at  $\beta = 2.00$  and 1.82, respectively. The measured masses for the pion and kaon,  $m_\pi$  and  $m_K$ , are presented in Table I. It is noted that the measured masses at each  $\beta$  are slightly different from the physical ones,  $m_{\pi^-} = 0.13957061 \text{ GeV}$  and  $m_{K^0} = 0.497611 \text{ GeV}$ , for the  $K_{\ell 3}$  decay in this calculation. In a later section, we will explain that the tiny differences are corrected using the next-to-leading order (NLO) SU(3) chiral perturbation theory (ChPT), and the corrections in  $f_+(0)$  are as small as or less than the statistical error.

For the calculation method of the form factors at  $\beta = 2.00$ , we follow the one in our previous calculation [12]. The matrix element in Eq.(3) is extracted from the ratio of 2- and

TABLE I. Parameters for the PACS10 gauge configurations.  $L$ ,  $T$ ,  $a$ , and  $N_{\text{conf}}$  represent the spatial and temporal extents, the lattice spacing, and the number of the configurations, respectively. The spatial extent in units of fm and the measured  $m_\pi$  and  $m_K$  are also tabulated.

$\beta$	$L^3 \times T$	$a^{-1}[\text{GeV}]$	$a$ [fm]	$L$ [fm]	$m_\pi$ [GeV]	$m_K$ [GeV]	$N_{\text{conf}}$
2.00	$160^3 \times 160$	3.1108(70)	0.063	10.1	0.13777(20)	0.50481(19)	20
1.82	$128^3 \times 128$	2.3162(44)	0.085	10.9	0.13511(72)	0.49709(35)	20

TABLE II. Parameters in the quark action at each  $\beta$ .  $\kappa_l$ ,  $\kappa_s$ ,  $c_{\text{SW}}$ ,  $\rho$ ,  $N_{\text{stout}}$  express the hopping parameter for the light and strange quarks, the coefficient of the clover term, the stout smearing parameter, and the number of the stout smearing, respectively.

$\beta$	$\kappa_l$	$\kappa_s$	$c_{\text{SW}}$	$\rho$	$N_{\text{stout}}$
2.00	0.125814	0.124925	1.02	0.1	6
1.82	0.126117	0.124902	1.11	0.1	6

3-point functions given as

$$C_L^\pi(\vec{p}, t - t_i) = \langle 0 | O_{\pi,L}(\vec{p}, t) (O_{\pi,L}^s(\vec{p}, t_i))^\dagger | 0 \rangle, \quad (5)$$

$$C_L^K(\vec{p}, t - t_i) = \langle 0 | O_{K,L}(\vec{p}, t) (O_{K,L}^s(\vec{p}, t_i))^\dagger | 0 \rangle, \quad (6)$$

$$C_{\mu,L}^{K\pi}(\vec{p}, t - t_i) = \langle 0 | O_{K,L}(\vec{0}, t_f) V_\mu(\vec{p}, t) (O_{\pi,L}^s(\vec{p}, t_i))^\dagger | 0 \rangle. \quad (7)$$

In the 3-point function  $C_{\mu,L}^{K\pi}$ ,  $t_i \leq t \leq t_f$  is assumed. The pion, kaon, and weak vector current operators are defined as

$$O_{\pi,L}(\vec{p}, t) = \sum_{\vec{x}} \bar{u}(\vec{x}, t) \gamma_5 d(\vec{x}, t) e^{i\vec{p}\cdot\vec{x}}, \quad (8)$$

$$O_{K,L}(\vec{p}, t) = \sum_{\vec{x}} \bar{s}(\vec{x}, t) \gamma_5 d(\vec{x}, t) e^{i\vec{p}\cdot\vec{x}}, \quad (9)$$

$$V_\mu(\vec{p}, t) = \sum_{\vec{x}} \bar{u}(\vec{x}, t) \gamma_\mu s(\vec{x}, t) e^{i\vec{p}\cdot\vec{x}}. \quad (10)$$

$q(\vec{x}, t)$  for  $q = u, d, s$  represents a local quark field, where the color and Dirac indices are omitted. The source operator  $O_{H,L}^s$  for  $H = \pi, K$  at the time slice  $t_i$  in Eqs. (5)–(7) is calculated by the  $Z(2) \otimes Z(2)$  random source [18], whose random numbers are spread in all

the color, spin, and spatial spaces. For example  $O_{\pi,L}^s$  is defined as,

$$O_{\pi,L}^s(\vec{p}, t) = \frac{1}{N_r} \sum_j \left[ \sum_{\vec{x}} \bar{u}(\vec{x}, t) \eta_j^\dagger(\vec{x}) e^{i\vec{p}\cdot\vec{x}} \right] \gamma_5 \left[ \sum_{\vec{y}} d(\vec{y}, t) \eta_j(\vec{y}) \right], \quad (11)$$

where  $N_r$  is the number of the random source, and the color and spin indices are omitted. The  $Z(2) \otimes Z(2)$  random source  $\eta_j(\vec{x})$  satisfies the following condition as,

$$\frac{1}{N_r} \sum_j \eta_j^\dagger(\vec{x}) \eta_j(\vec{y}) \xrightarrow{N_r \rightarrow \infty} \delta(\vec{x} - \vec{y}). \quad (12)$$

Since this source reduces to the local operator when  $N_r$  is large enough, we shall call it as the local source operator.

At  $\beta = 2.00$ , we also employ the exponentially smeared quark operator with the Coulomb gauge fixed configuration in the calculations for the 2- and 3-point functions, defined as,

$$q_S(\vec{x}, t) = \sum_{\vec{y}} \phi(|\vec{y} - \vec{x}|) q(\vec{x}, t). \quad (13)$$

The smearing function  $\phi(r)$  is given with the spatial extent of  $L$  as

$$\phi(r) = \begin{cases} 1 & (r = 0) \\ Ae^{-Br} & (r < L/2) \\ 0 & (r \geq L/2) \end{cases}. \quad (14)$$

The smearing parameters for the light and strange quarks are chosen as  $(A, B) = (1.2, 0.14)$  and  $(1.2, 0.22)$ , respectively, to obtain earlier plateaus in the effective meson masses. In the smeared operator calculation, all the quark fields  $u, d, s$  in the meson operators in the 2- and 3-point functions, *i.e.*,  $O_{H,L}$  and  $O_{H,L}^s$  for  $H = \pi, K$ , are replaced by  $u_S, d_S, s_S$ . On the other hand, the quark fields in the vector current are unchanged. In the following we will denote the meson operators and the correlators with the exponentially smeared operator as  $O_{H,S}, O_{H,S}^s, C_S^\pi, C_S^K$ , and  $C_{\mu,S}^{K\pi}$ .

In order to estimate the form factors in the continuum limit, another 3-point function is calculated with the point splitting conserved vector current, which is given by

$$\tilde{V}_\mu(\vec{p}, t) = \sum_{\vec{x}} \bar{u}(\vec{x}, t) \tilde{\gamma}_\mu(\vec{x}, t) s(\vec{x}, t) e^{i\vec{p}\cdot\vec{x}}, \quad (15)$$

where

$$\tilde{f}(x) \tilde{\gamma}_\mu(x) g(x) = \frac{1}{2} [\bar{f}(x + \hat{\mu})(1 + \gamma_\mu) U_\mu^\dagger(x) g(x) - \bar{f}(x)(1 - \gamma_\mu) U_\mu(x) g(x + \hat{\mu})] \quad (16)$$



with  $x$  expresses a four-dimensional vector of  $(\vec{x}, t)$ . The 3-point function with the conserved current is represented by  $\tilde{C}_{\mu, X}^{K\pi}$  for  $X = L, S$ . In all the cases the 3-point functions are measured using the sequential source method at the sink time slice  $t_f$ .

The conserved current data at  $\beta = 1.82$  is newly added in this work, which was not calculated in our previous work [12]. It is noted that only the local operator is employed in the measurements for the 2- and 3-point functions at this lattice spacing.

The periodic boundary condition in the spatial directions is employed in the calculation of quark propagators. As in our previous work [12], we average the correlators with the periodic and anti-periodic boundary conditions in the temporal direction. This average reduces unwanted wrapping around effects in the 3-point functions [19], and also makes the periodicity of the 2-point functions effectively double. In the correlators with the anti-periodic boundary condition, one of the quark propagators in Eqs. (5)–(7) is computed with the temporal anti-periodic boundary condition as explained in Ref. [12]. All the correlators are regarded as the averaged ones in the following discussion, unless otherwise explicitly stated.

The momentum is labeled by an integer  $n_p$  as  $p^2 = \bar{p}^2 = (2\pi/L)^2 n_p$ . We employ  $0 \leq n_p \leq 6$  to obtain the form factors in the vicinity of  $q^2 = 0$ . For a finite momentum case, we compute the correlators with several momentum assignments to increase statistics.  $q^2$  is evaluated with

$$q^2 = -(m_K - E_\pi(p))^2 + p^2 \quad (17)$$

where  $E_\pi(p) = \sqrt{m_\pi^2 + (2\pi/L)^2 n_p}$  with the measured  $m_\pi$ . At each  $\beta$  the values of  $q_{n_p}^2$  denoting  $q^2$  with  $n_p$  are tabulated in Table III as well as the number of the momentum assignment.

We investigate the current time dependence of the 3-point function using several time separations between the source and sink operators,  $t_{\text{sep}} = t_f - t_i$  in Eq. (7). The values of  $t_{\text{sep}}$  employed in our calculation are tabulated in Table IV. The same set of  $t_{\text{sep}}$  is used in the 3-point functions with both the local and conserved vector currents. It is noted that we employ shorter  $t_{\text{sep}}$  in the smeared operator calculation than the one in the local case at  $\beta = 2.00$ , because excited state effects are well suppressed by the smearing.

Using the same techniques in Ref. [12], the signal of the correlators is improved by repeating the calculation on each configuration with 4 temporal directions by rotating the configuration thanks to the hypercube symmetry, and averaging a backward 3-point func-

TABLE III. The value of the momentum transfer squared  $q_{n_p}^2$  [GeV<sup>2</sup>] at each  $\beta$  and  $n_p = (L/2\pi)^2 p^2$ .  $\nu_p$  is the number of the momentum assignment in the calculation of the correlators.

$\beta$	$q_0^2$	$q_1^2$	$q_2^2$	$q_3^2$	$q_4^2$	$q_5^2$	$q_6^2$
2.00	-0.13471(23)	-0.08791(18)	-0.05072(15)	-0.01889(13)	0.00938(11)	0.03507(10)	0.05878(8)
1.82	-0.13103(48)	-0.08980(33)	-0.05656(25)	-0.02792(20)	-0.00239(17)	0.02087(15)	0.04239(13)
$\nu_p$	1	6	12	8	6	9	9

TABLE IV. The source-sink separation  $t_{\text{sep}} = t_f - t_i$  of the 3-point function in lattice and physical units at each  $\beta$  for local and smeared operators. The numbers of measurements  $N_{\text{meas}}$ <sup>a</sup> for the correlators are also presented.

$\beta$	2.00		1.82
operator	local	smeared	local
$t_{\text{sep}}$	(50, 58, 64)	(36, 42, 48, 54)	(36, 42, 48)
$t_{\text{sep}}$ [fm]	(3.2, 3.7, 4.1)	(2.3, 2.7, 3.0, 3.4)	(3.1, 3.6, 4.1)
$N_{\text{meas}}$	(1280, 2560, 1280)	(640, 1280, 2560, 1280)	(1280, 2560, 2560)

<sup>a</sup> We adopt a different counting rule of measurement from that in the previous paper [12]. Thus,  $N_{\text{meas}}$  at  $\beta = 1.82$  becomes half of the previous paper, though it means the same.

tion in  $t_f \leq t \leq t_i$  with the same  $t_{\text{sep}}$ . We also adopt calculations with different 8 source time slices in equally separated 20 and 16 time intervals at  $\beta = 2.00$  and 1.82, respectively, except for  $t_{\text{sep}} = 36$  with the smeared operator calculation at  $\beta = 2.00$ , where different 4 source time slices with 40 separations are employed. The number of the random source  $N_r$  in Eq. (12) is unity in almost all the cases, while  $N_r = 2$  is used in larger  $t_{\text{sep}}$  cases: the local and smeared operator calculations with  $t_{\text{sep}} = 58$  and 48 at  $\beta = 2.00$ , respectively, and  $t_{\text{sep}} = 42, 48$  at  $\beta = 1.82$ . The total numbers of measurement are summarized in Table IV.

### C. Extraction of matrix element

First, we focus on the calculation with the local vector current, and the analysis method to extract the matrix element from the data at  $\beta = 2.00$  is explained below.

The matrix element in Eq. (3) is obtained from the ground state contribution in the

3-point function. Its time dependence differs from excited state contributions. To extract the matrix element, we define a ratio  $R_{\mu,X}(t; n_p)$  as,

$$R_{\mu,X}(t; n_p) = Z_X^\pi(p) Z_X^K(0) \frac{N_\mu(\vec{p}) C_{\mu,X}^{K\pi}(\vec{p}, t)}{C_X^\pi(\vec{p}, t) C_X^K(\vec{0}, t_{\text{sep}} - t)}, \quad (18)$$

at each  $p^2 = (2\pi/L)^2 n_p$  for  $X = L, S$ . In the equation it is assumed  $t_i = 0$ , which is also employed in the following discussion. The coefficient  $N_\mu$  is defined by  $N_4(\vec{p}) = 1$  and  $N_i(\vec{p}) = 1/p_i$  with  $i = 1, 2, 3$ , and  $Z_X^\pi(p)$  and  $Z_X^K(0)$  are determined from fitting of the 2-point functions in a large  $t$  region using a fit form given by

$$C_X^H(\vec{p}, t) = \frac{(Z_X^H(p))^2}{2E_H(p)} (e^{-E_H(p)t} + e^{-E_H(p)(2T-t)}), \quad (19)$$

with  $E_H(p) = \sqrt{m_H^2 + p^2}$  for  $H = \pi, K$ . Noted that  $C_X^H$  and  $C_{\mu,X}^{K\pi}$  have the  $2T$  periodicity, since they are calculated by average of periodic and anti-periodic correlators in the temporal direction as explained in the last subsection. In the local operator calculation ( $X = L$ ), we use the relation  $Z_L^\pi(p) = Z_L^\pi(0)$ , which is confirmed statistically.

In a middle time region,  $0 \ll t \ll t_{\text{sep}}$ ,  $R_{\mu,X}$  behaves as,

$$R_{\mu,X}(t; n_p) = R_\mu(p) + \Delta A_{\mu,X}(p, t), \quad (20)$$

where the constant part corresponds to the matrix element  $R_\mu(p) = \frac{N_\mu(\vec{p})}{Z_V} \langle \pi(\vec{p}) | V_\mu | K(\vec{0}) \rangle$  with  $p^2 = (2\pi/L)^2 n_p$ . The last term on the right-hand side represents the leading contribution from excited states. In a later section, its functional form is discussed to extract the matrix elements. The renormalization factor of the local vector current  $Z_V$  is determined from a ratio with 3-point functions for  $\pi$  and  $K$  electromagnetic form factors at  $q^2 = 0$  as,

$$R_{Z_V}(t) = \sqrt{\frac{C_X^\pi(\vec{0}, t_{\text{sep}}) C_X^K(\vec{0}, t_{\text{sep}})}{C_{4,X}^{\pi\pi}(t) C_{4,X}^{KK}(t)}}. \quad (21)$$

The correlators are defined by

$$C_{4,X}^{\pi\pi}(t) = \left\langle 0 \left| O_{\pi,X}(\vec{0}, t_{\text{sep}}) V_4^{\text{em}}(\vec{0}, t) \left( O_{\pi,X}^s(\vec{0}, 0) \right)^\dagger \right| 0 \right\rangle, \quad (22)$$

$$C_{4,X}^{KK}(t) = \left\langle 0 \left| O_{K,X}(\vec{0}, t_{\text{sep}}) V_4^{\text{em}}(\vec{0}, t) \left( O_{K,X}^s(\vec{0}, 0) \right)^\dagger \right| 0 \right\rangle, \quad (23)$$

where  $V_4^{\text{em}}(t)$  is the temporal component of the local electromagnetic current.

Typical data of  $R_{Z_V}$  at  $\beta = 2.00$  using the local and smeared operators in  $t_{\text{sep}} = 50$  and 42, respectively, are shown in Fig. 1. From a constant fit in a flat region of the smeared

operator data, we obtain  $Z_V = 0.971840(96)$ . This value agrees with the one obtained from the other operator calculation in the figure,  $Z_V = 0.97190(11)$ . Those are also statistically consistent with results obtained from other  $t_{\text{sep}}$  data using the local and smeared operators. The value of the smeared operator is adopted in the following analysis at  $\beta = 2.00$ .

At  $\beta = 1.82$  we use  $Z_V$  from the local operator calculation to adopt the common setups as in  $\beta = 2.00$ , although the difference of  $Z_V$  obtained from the local operator calculation and the Schrödinger functional scheme [20] was discussed in Ref. [12].

In the case of the 3-point function with the conserved vector current, the calculation strategy is basically the same as above. The difference is only that  $Z_V = 1$  is employed. We confirm that  $Z_V$  of the conserved vector current statistically agrees with unity by the same calculation as in Eq. (21), but using  $\tilde{C}_{4,X}^{\pi\pi}$  and  $\tilde{C}_{4,X}^{\pi\pi}$  calculated with the conserved electromagnetic vector current.

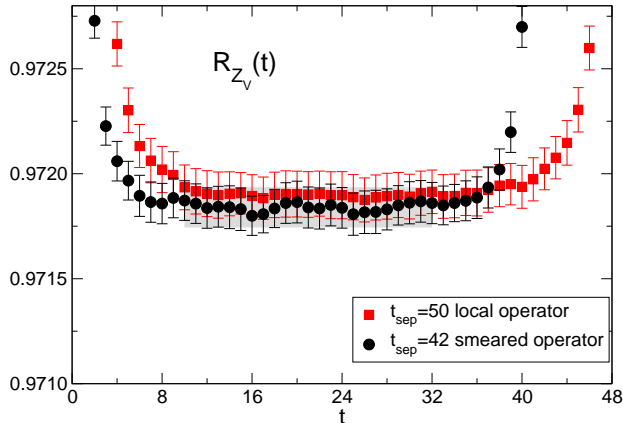


FIG. 1. Ratios defined in Eq. (21) for the local (square) and smeared (circle) data in  $t_{\text{sep}} = 50$  and 42, respectively, as a function of  $t$ . The shaded band represents a constant fit result of the smeared data with one standard deviation, which corresponds to the value of  $Z_V$ .

### III. RESULT AT FINITE LATTICE SPACINGS

In this section we will present results of the form factors at  $\beta = 2.00$  and 1.82. First, the results using the local vector current at only  $\beta = 2.00$  are described, because those at  $\beta = 1.82$  are already reported in Ref. [12]. And then the results from the conserved vector current at both the lattice spacings are discussed.

### A. Local current result at $\beta = 2.00$

In this subsection the data calculated with the local vector current at  $\beta = 2.00$  are presented. They are calculated using the local and smeared operators.

The wrapping around effects in the 3-point functions are suppressed by averaging the correlators with two boundary conditions, as discussed in our previous work [12]. A similar effect of the suppression is seen in this calculation. The left panel of Fig. 2 shows the two ratios  $R_{4,L}(t;0)$  using the local operator with  $t_{\text{sep}} = 58$  defined in Eq. (18), but using  $C_{4,L}^{K\pi}$  with the periodic and anti-periodic boundary conditions in the temporal direction represented by circle and square symbols, respectively. The two data have different time dependence in the middle region,  $0 \ll t \ll t_{\text{sep}}$ . It is considered to be caused by wrapping around effects, which is similar to the ones in Ref. [19]. The average with the two data denoted by diamonds gives a mild  $t$  dependence in the same region, because the effects are effectively canceled out in the average. The wrapping around effects become smaller as the momentum increases shown in the right panel of Fig. 2. The same trend was seen in our previous work [12]. Figure 3 presents that a similar suppression is observed in the smeared operator calculation with  $t_{\text{sep}} = 48$ , though the wrapping around effects seem relatively smaller than the local operator case. As explained in the previous section, the averaged data are employed in the following analyses.

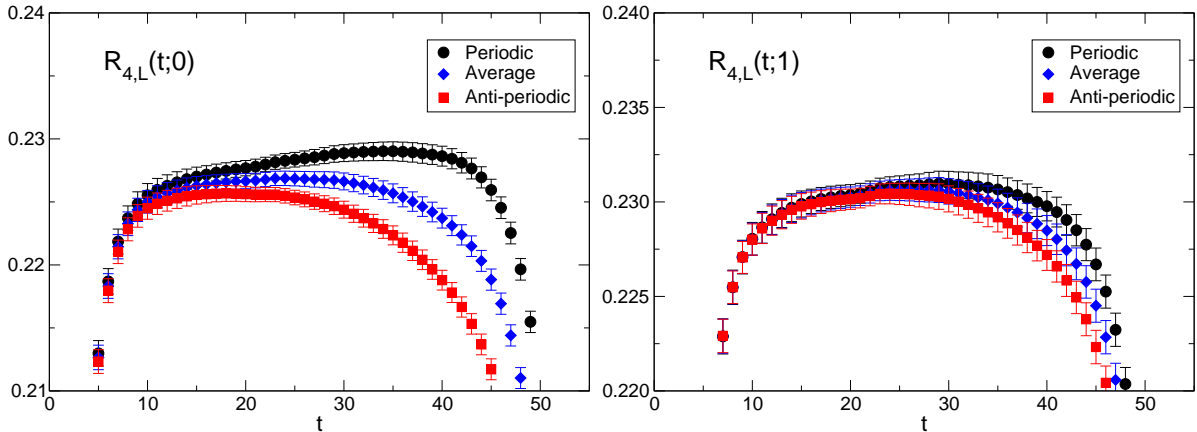


FIG. 2. Ratios  $R_{4,L}(t; n_p)$  with  $t_{\text{sep}} = 58$  defined in Eq.(18) for  $n_p = 0$  and 1 correspond to the left and right panels, respectively. The ratios calculated from the 3-point function with the periodic and anti-periodic boundary conditions in the temporal direction are expressed by circle and square symbols. Their average is also shown by diamond symbol.

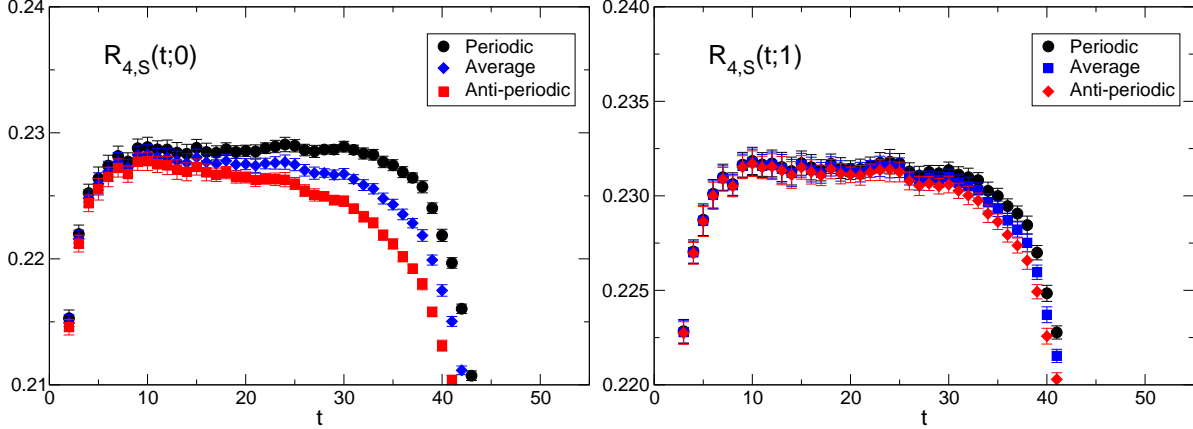


FIG. 3. The same figure as Fig. 2, but for  $R_{4,S}$  with  $t_{\text{sep}} = 48$ .

In order to extract the constant part in  $R_{\mu,X}$ , which is  $R_{\mu}(p)$  in Eq. (20) corresponding to the matrix element,  $R_{\mu,X}$  in a middle  $t$  region is fitted by a fitting form given in Eq. (20) with an appropriate leading excited state term  $\Delta A_{\mu,X}$ . We adopt the same form of  $\Delta A_{\mu,X}$  as in our previous calculation [12] given by

$$\Delta A_{\mu,X}(p, t) = A_{\mu,X}^{\pi}(p)e^{-\Delta_{\pi}(p)t} + A_{\mu,X}^K(p)e^{-\Delta_K(t_f-t)}. \quad (24)$$

In the local operator case we choose

$$\Delta_{\pi}(p) = \sqrt{(m'_{\pi})^2 + p^2} - E_{\pi}(p), \quad (25)$$

$$\Delta_K = m'_K - m_K. \quad (26)$$

The value of  $m'_H$  is fixed by the experimental value of the first excited state mass of the  $H$  meson,  $m'_{\pi} = 1.3$  GeV and  $m'_K = 1.46$  GeV in PDG20 [1]. This is because the first excited masses estimated from our 2-point functions with the local operator presented in Fig. 4 are well consistent with those values, albeit the errors are large. The analysis method to extract the first excited state mass from the 2-point function with the local operator is the same as explained in the previous work [12]. On the other hand,  $\Delta_{\pi}(p)$  and  $\Delta_K$  are chosen as free parameters in the smeared operator data.

We carry out a simultaneous fit using all the  $t_{\text{sep}}$  data with both the operators to obtain a common  $R_{\mu}(p)$ . As a typical example of the fit result, the results from  $R_{4,L}(t;1)$  and  $R_{4,S}(t;1)$  are plotted in Fig. 5. The fit ranges are chosen such that the value of the uncorrelated  $\chi^2/\text{dof}$  is less than unity. The minimum time  $t_{\text{min}}$  of the fit range is fixed, while the maximum is shifted by  $t_{\text{max}} = t_{\text{sep}} - t_{\text{fit}}$ . The choice of  $t_{\text{min}}$  and  $t_{\text{max}}$  depends on the operator. In the figure,

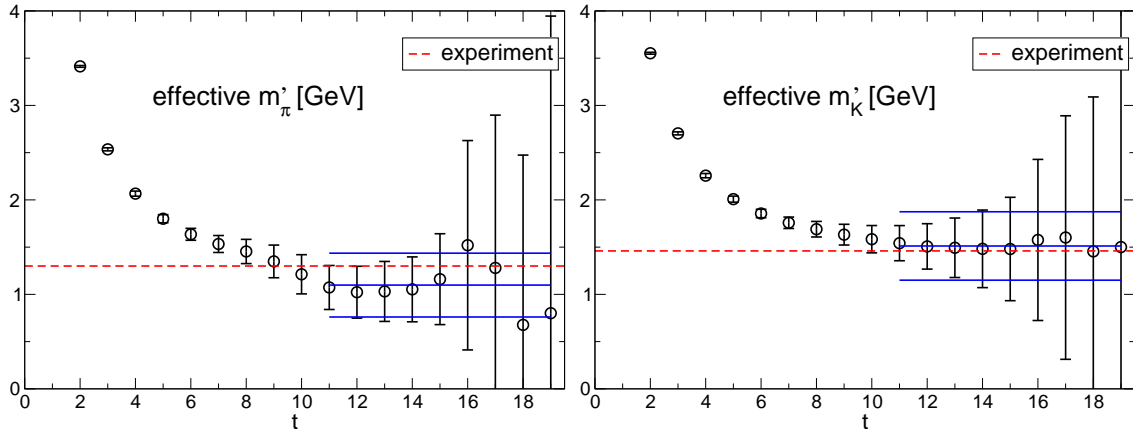


FIG. 4. Effective masses of the first excited state for  $\pi$  (left) and  $K$  (right) in GeV units. The dashed lines correspond to their experimental values. The solid lines express a fit result with one standard deviation, and their lengths represent the fit range.

we employ  $(t_{\min}, t_{\text{fit}}) = (8, 16)$  and  $(2, 8)$  for the local and smeared operators, respectively. The fit curves well explain our data in the middle  $t$  region for both the operators. From the fit we extract  $R_4(p)$  denoted by the light blue band in the figure, which agrees with the larger  $t_{\text{sep}}$  data in the middle region. Noted that the value of  $\chi^2/\text{dof}$  is not so tiny even in uncorrelated fits, because the smeared operator data do not behave as a smooth function of  $t$  as shown in the right panel of Fig. 5. It seems to be caused by a weak correlation among the data in the different time slices. Another reason of the large  $\chi^2/\text{dof}$  might be a weak correlation among the different operator data, which are calculated with different random sources in each source operator.

The spatial component of the matrix element  $R_i(p)$  is extracted from the same simultaneous fit using the two operator data. The data of the spatial component are obtained by the average of  $R_{i,X}(t; n_p)$  in  $i = 1, 2, 3$  at each  $n_p$  and  $X$ . Figure 6 shows that the data for  $R_{i,L}(t; 1)$  and  $R_{i,S}(t; 1)$  have rather larger statistical fluctuations than those for  $\mu = 4$ . Using  $(t_{\min}, t_{\text{fit}}) = (8, 22)$  and  $(2, 9)$  for the local and smeared operators, a reasonable fit can be carried out represented by gray curves, and the result of  $R_i(p)$  is expressed by a light blue band in the figure.

In the  $\mu = 4$  and  $i$  cases, we also carry out another analysis using free exponents in  $\Delta A_{\mu,L}$  instead of the fixed ones. The results from the two analyses agree with each other within the statistical error. Furthermore, a two-exponential fit analysis is performed, where another

excited state term  $\Delta B_{\mu,X}(p,t)$  with the same form as  $\Delta A_{\mu,X}(p,t)$  in Eq. (24) is added in a fit function, which is given as

$$R_{\mu,X}(t; n_p) = R_{\mu}(p) + \Delta A_{\mu,X}(p,t) + \Delta B_{\mu,X}(p,t). \quad (27)$$

Since in general a two-exponential fit is numerically unstable, in this analysis, the exponents in  $\Delta A_{\mu,X}$  are fixed as above for both the operators  $X = L, S$ , while those in  $\Delta B_{\mu,X}$  are free parameters. The results from the two-exponential analysis are statistically consistent with those from the above analyses, although the statistical errors are larger.

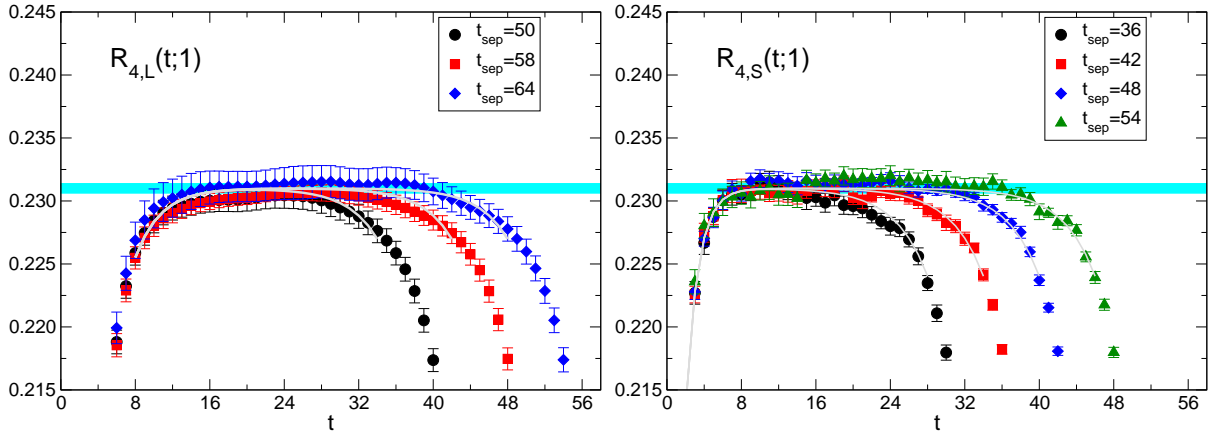


FIG. 5. Ratios  $R_{4,X}(t;1)$  defined in Eq.(18) for the local  $X = L$  (left) and smeared  $X = S$  (right) operators. Different symbols express different  $t_{\text{sep}}$  data in each panel. The gray curves correspond to results from a simultaneous fit. The light blue band is the result of the matrix element  $R_4(p)$ .

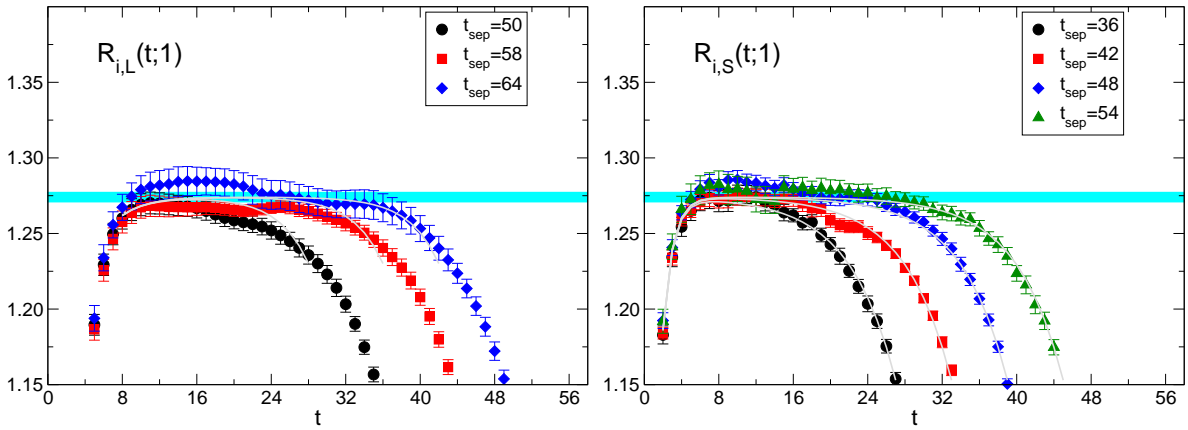


FIG. 6. The same figure as Fig. 5, but for  $R_{i,X}(t;1)$ .

The bare matrix elements obtained from the above fits are renormalized with  $Z_V$  discussed



in the previous section. Using the matrix elements in  $\mu = 4$  and  $i$ , the form factors  $f_+$  and  $f_0$  are determined by solving a linear equation at each  $q_{n_p}^2$ . The results for the form factors are plotted in Fig. 7 as a function of  $q^2$ . We also perform similar analyses explained above with only the local or smeared operator data to study a stability of our result. As shown in the figure, their results are in good agreement with those from the combined analysis using both the operator data discussed above. The values for the form factors from all the analyses are tabulated in Table V. In the combined analysis, the values of  $\xi(q^2) = f_-(q^2)/f_+(q^2)$  are also listed. We note that the relative difference between the form factors from the local and smeared operators is at most  $1.6 \sigma$ . It can be mainly caused by poor statistics in our calculation. As presented in Table V, the error of the combined analysis is smaller than those in the two operator data, especially in the larger  $q^2$ . While we suspect a reason is that the correlation between the local and smeared data becomes weaker as  $q^2$  increase, we would need more detailed studies to clarify a reason of the error reduction. In this paper, our main result is obtained from the combined analysis, while a systematic error is estimated using the other two results.

The form factors are compared with those at  $\beta = 1.82$  obtained in our previous work [12]. Figure 8 shows that two data of  $f_+$  at the different lattice spacings are well consistent with each other in all  $q^2$  region we measured. It means that finite lattice spacing effects in  $f_+$  seem small. A similar consistency is observed in  $f_0$  near  $q^2 = 0$ , while a little difference is seen in a negative  $q^2$  region. In a later section, we will chose a fit form of the finite lattice spacing effects in a continuum extrapolation based on this tendency.

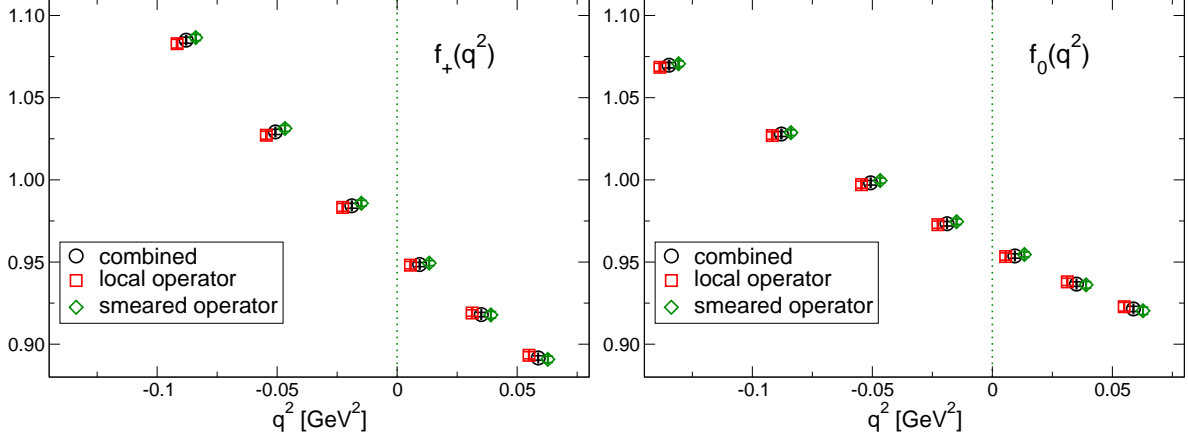


FIG. 7.  $K_{\ell 3}$  form factors  $f_+(q^2)$  (left) and  $f_0(q^2)$  (right) obtained from the local and smeared operators, and also combined analysis using both the operators. Those data are expressed by square, diamond, and circle symbols. The results are obtained from the local current data. The square and diamond symbols are slightly shifted to the negative and positive  $x$  direction, respectively, for clarity.

TABLE V. Results for the form factors  $f_+(q^2)$  and  $f_0(q^2)$  in each  $q^2$  at  $\beta = 2.00$  using the local vector current with the combined analysis, local, and smeared operator data, respectively. The ratio  $\xi(q^2) = f_-(q^2)/f_+(q^2)$  is also presented in the combined analysis.

$q^2$	combined			local		smeared	
	$f_+(q^2)$	$f_0(q^2)$	$\xi(q^2)$	$f_+(q^2)$	$f_0(q^2)$	$f_+(q^2)$	$f_0(q^2)$
$q_0^2$	...	1.0697(17)	...	...	1.0685(24)	...	1.0707(17)
$q_1^2$	1.0850(18)	1.0279(15)	-0.1412(11)	1.0829(27)	1.0270(22)	1.0866(18)	1.0288(17)
$q_2^2$	1.0292(16)	0.9982(14)	-0.1400(12)	1.0271(24)	0.9971(21)	1.0313(18)	0.9996(15)
$q_3^2$	0.9842(15)	0.9733(14)	-0.1384(16)	0.9833(24)	0.9727(22)	0.9858(18)	0.9746(16)
$q_4^2$	0.9485(13)	0.9537(13)	-0.1380(33)	0.9481(22)	0.9533(22)	0.9493(15)	0.9546(15)
$q_5^2$	0.9180(13)	0.9366(14)	-0.1360(29)	0.9190(20)	0.9379(22)	0.9178(20)	0.9361(20)
$q_6^2$	0.8916(14)	0.9215(16)	-0.1342(46)	0.8933(22)	0.9228(26)	0.8908(19)	0.9203(23)

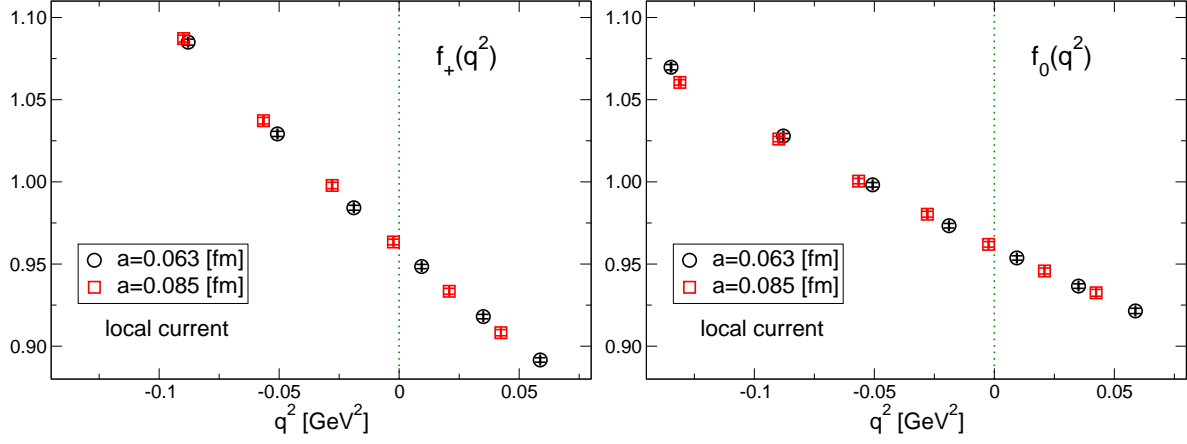


FIG. 8. Comparisons for  $K_{\ell 3}$  form factors  $f_+(q^2)$  (left) and  $f_0(q^2)$  (right) at the two lattice spacings obtained from the local current data. The data at the fine and coarse lattice spacings are expressed by circle and square symbols, respectively.

## B. Conserved current result

As in the local current data discussed in the above, the form factors at  $\beta = 2.00$  are extracted from the 3-point functions with the conserved vector current by the same analysis method described in Sec. III A. The obtained results for the form factors from the combined analysis are shown in Table VI together with those from the local or smeared operator data. As in the local current case, we confirm that the relative difference between the form factors from the local and smeared operators is less than  $1.5 \sigma$ . The three results are in good agreement with each other. The error reduction of the combined analysis compared to the two operator data is observed in large  $q^2$  region, which might be caused by a weak correlation between the local and smeared operator data as discussed in the previous subsection.

At  $\beta = 1.82$ , the form factors with the conserved vector current are calculated using only the local operator data as in our previous calculation [12]. The analysis method is the same as that in the previous one, which is also the same as the local operator data analysis at  $\beta = 2.00$ , where  $\Delta_\pi(p)$  and  $\Delta_K$  in  $\Delta A_{\mu,L}$  defined in Eq. (24) are fixed by the experimental values of the first excited meson masses. We also perform an extra analysis with  $\Delta_\pi(p)$  and  $\Delta_K$  as free parameters. In the following the two choices are called “A1” and “A2,” respectively, as in the previous work [12]. The values for the form factors obtained from both the analyses are tabulated in Table VII. The statistical errors in the A2 analysis are larger than those in the A1 analysis especially at the largest  $q^2$ . The same trend was observed in the local current data in Ref. [12]. The A1 result is used in our main analysis, while A2 is adopted for estimate of systematic error, explained in a later section.

The data at the different lattice spacings are compared in each form factor as shown in Fig. 9. In contrast to the local current data in Fig. 8, small finite lattice spacing effects are observed in the vicinity of  $q^2 = 0$  for both the form factors, and these effects seem to increase with  $q^2$  in both the form factors.

## C. Interpolation in finite lattice spacing

Before discussing the continuum extrapolation using the data at the two lattice spacings, a  $q^2$  interpolation at each lattice spacing is performed to investigate a lattice spacing dependence of each form factor in this subsection. We analyze the data using the combined and

TABLE VI. The same table as Table V, but for the conserved vector current at  $\beta = 2.00$ .

$q^2$	combined			local		smeared	
	$f_+(q^2)$	$f_0(q^2)$	$\xi(q^2)$	$f_+(q^2)$	$f_0(q^2)$	$f_+(q^2)$	$f_0(q^2)$
$q_0^2$	...	1.0819(17)	...	...	1.0807(24)	...	1.0828(17)
$q_1^2$	1.0858(18)	1.0391(15)	-0.1153(11)	1.0837(26)	1.0382(23)	1.0873(18)	1.0400(17)
$q_2^2$	1.0340(16)	1.0088(14)	-0.1137(13)	1.0320(24)	1.0077(21)	1.0361(18)	1.0101(15)
$q_3^2$	0.9923(15)	0.9834(14)	-0.1118(16)	0.9913(24)	0.9828(22)	0.9938(18)	0.9845(17)
$q_4^2$	0.9591(13)	0.9633(13)	-0.1105(33)	0.9587(23)	0.9629(23)	0.9599(15)	0.9642(15)
$q_5^2$	0.9308(15)	0.9459(16)	-0.1092(29)	0.9317(20)	0.9471(22)	0.9306(20)	0.9454(19)
$q_6^2$	0.9065(14)	0.9307(16)	-0.1072(46)	0.9078(22)	0.9317(27)	0.9058(20)	0.9298(24)

TABLE VII. Results for the form factors  $f_+(q^2)$  and  $f_0(q^2)$  in each  $q^2$  at  $\beta = 1.82$  using the conserved vector current. The meaning for the A1 and A2 analyses are the same as in Ref. [12]. The ratio  $\xi(q^2) = f_-(q^2)/f_+(q^2)$  is also presented in the A1 analysis.

$q^2$	A1			A2	
	$f_+(q^2)$	$f_0(q^2)$	$\xi(q^2)$	$f_+(q^2)$	$f_0(q^2)$
$q_0^2$	...	1.0781(17)	...	...	1.0785(16)
$q_1^2$	1.0885(21)	1.0423(16)	-0.1082(14)	1.0893(24)	1.0426(17)
$q_2^2$	1.0435(20)	1.0157(17)	-0.1078(20)	1.0459(32)	1.0167(20)
$q_3^2$	1.0081(19)	0.9948(18)	-0.1078(25)	1.0108(36)	0.9966(27)
$q_4^2$	0.9768(17)	0.9758(17)	-0.1059(32)	0.9779(25)	0.9767(25)
$q_5^2$	0.9497(18)	0.9591(18)	-0.1083(33)	0.9506(22)	0.9604(25)
$q_6^2$	0.9269(19)	0.9453(21)	-0.1070(46)	0.9304(45)	0.9521(76)

A1 analyses at  $\beta = 2.00$  and  $1.82$ , respectively, in both the local and conserved currents. Those values are presented above, while the local current data at  $\beta = 1.82$  are reported in Table II of Ref. [12].

An interpolation of the form factors to  $q^2 = 0$  is performed with the same fitting forms as in our previous work [12]. They are based on the NLO SU(3) ChPT, and we add correction

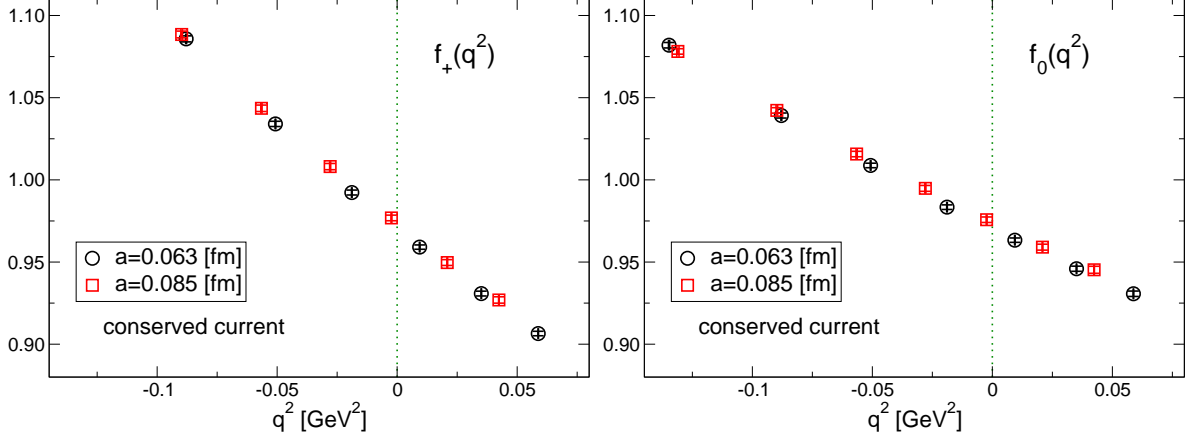


FIG. 9. The same figure as Fig. 8, but for the conserved vector current data.

terms as,

$$f_+(q^2) = 1 - \frac{4}{F_0^2} L_9 q^2 + K_+(q^2) + c_0 + c_2^+ q^4, \quad (28)$$

$$f_0(q^2) = 1 - \frac{8}{F_0^2} L_5 q^2 + K_0(q^2) + c_0 + c_2^0 q^4, \quad (29)$$

where  $F_0$  is the pion decay constant<sup>1</sup> in the SU(3) chiral limit. The NLO functions  $K_+(q^2)$  and  $K_0(q^2)$  are given in Refs. [21, 22], which depend on  $m_\pi$ ,  $m_K$ ,  $q^2$ ,  $F_0$ , and the scale  $\mu = 0.77$  GeV. Their explicit forms are shown in Appendix A of Ref. [12], and they satisfy  $K_+(0) = K_0(0)$ .  $L_9$ ,  $L_5$ ,  $c_0$ , and  $c_2^{+,0}$  are free parameters in a fit. A common  $c_0$  is employed to satisfy the constraint of  $f_+(0) = f_0(0)$ . The last two terms in both the equations may be considered as a part of the NNLO analytic terms in the SU(3) ChPT.

We employ a fixed value of  $F_0 = 0.11205$  GeV<sup>2</sup> in interpolations as in Ref. [12]. The fit results are presented in Figs. 10 and 11 for the local current at  $\beta = 2.00$  and the conserved current at both  $\beta$ , respectively. All the fits well explain our data. The values for the fit parameters and the uncorrelated  $\chi^2/\text{dof}$  are tabulated in Table VIII together with the results obtained from the same fit of the local current data at  $\beta = 1.82$  [12] for comparison. In the local current, the results for  $f_+(0)$  and  $L_9$  are well consistent at the different lattice spacings, which is expected from the consistency of  $f_+(q^2)$  at the different lattice spacings presented in the left panel of Fig. 8.

<sup>1</sup> We adopt the normalization of  $F_\pi \sim 132$  MeV at the physical point.

<sup>2</sup>  $F_0$  is determined from the average of ratios,  $F/F_0 = 1.229(59)$  [23] and  $F/F_0 = 1.078(44)$  [24], and the pion decay constant of the SU(2) ChPT in the chiral limit  $F = 0.12925$  GeV, which was calculated at  $\beta = 1.82$  [25, 26].

Using the fit results a tiny chiral extrapolation to the physical point,  $m_{\pi^-} = 0.13957061$  GeV and  $m_{K^0} = 0.497611$  GeV, is carried out at each data. The value at the physical point is evaluated by replacing  $m_{\pi}$  and  $m_K$  in the functions  $K_+$  and  $K_0$  in Eqs. (28) and (29) by  $m_{\pi^-}$  and  $m_{K^0}$ . Due to the short extrapolation, we neglect the mass dependences of the last two terms in Eqs. (28) and (29). The evaluated value of  $f_+(0)$  at the physical point is presented in Table IX. Comparing with the values of  $f_+(0)$  at each  $\beta$  in between Tables VIII and IX, it is found that the corrections of the chiral extrapolation are as small as or less than the statistical error. The slope and curvature of the form factors defined by

$$\lambda'_s = \frac{m_{\pi^-}^2}{f_+(0)} \left. \frac{df_s(q^2)}{d(-q^2)} \right|_{q^2=0}, \quad (30)$$

$$\lambda''_s = \frac{m_{\pi^-}^4}{f_+(0)} \left. \frac{d^2f_s(q^2)}{d(-q^2)^2} \right|_{q^2=0}, \quad (31)$$

for  $s = +, 0$  are also calculated using the fit results at the physical point. Those results are compiled in Table IX.

Here, we discuss the lattice spacing dependence of the physical quantities listed in Table IX. Each result of  $f_+(0)$  is plotted in Fig. 12 as a function of the lattice spacing  $a$ . The result of the local current has a mild  $a$  dependence, while that of the conserved current almost behaves as a linear function. A similar tendency was observed in the hadron vacuum polarization calculation with the local and conserved vector currents on the PACS10 configurations [16]. It is expected that the value in the continuum limit could be in between the two current data at the smaller lattice spacing, and the two current data converge in the continuum limit. Based on this observation, we will choose fitting forms of the form factor for the continuum extrapolation in the next section.

A similar split between the local and conserved current data is observed in the result of  $\lambda'_+$  shown in the left panel of Fig. 13. In contrast to  $f_+(0)$  and  $\lambda'_+$ , the difference between the local and conserved current results is not clear at each lattice spacing as presented in the right panel of Fig. 13 for  $\lambda'_0$ , and Fig. 14 for  $\lambda''_+$  and  $\lambda''_0$ . These three quantities have large fitting form dependences in the continuum extrapolation, which will be discussed in the next section.

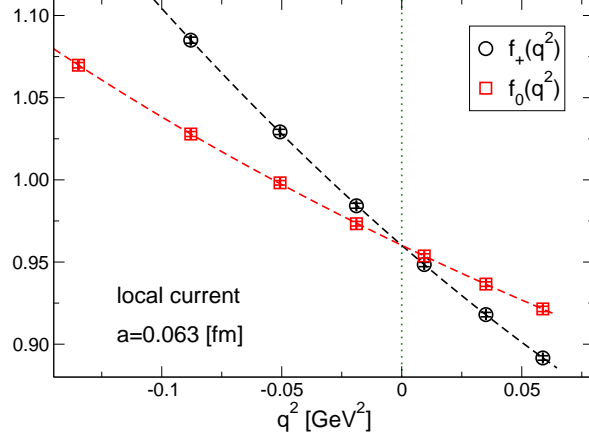


FIG. 10. Interpolation of  $K_{\ell 3}$  form factors  $f_+(q^2)$  and  $f_0(q^2)$  to  $q^2 = 0$  with fit forms based on the NLO SU(3) ChPT formulas in Eqs. (28) and (29) using the local vector current data at  $\beta = 2.00$ . The dashed curves express results from a simultaneous fit using  $f_+(q^2)$  and  $f_0(q^2)$  data.

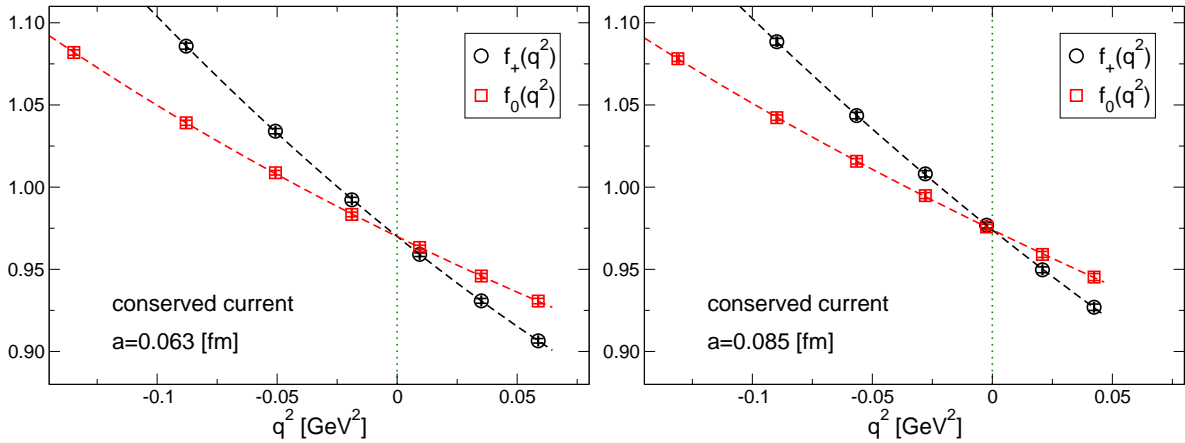


FIG. 11. The same figure as Fig. 10, but using the conserved vector current data at  $\beta = 2.00$  (left) and 1.82 (right).



TABLE VIII. Fit results of  $K_{\ell 3}$  form factors based on the NLO SU(3) ChPT formulas in Eqs. (28) and (29) with the local and conserved vector currents at each  $\beta$  together with the value of the uncorrelated  $\chi^2/\text{dof}$ .  $F_0$  is fixed in all the fits. The result with the local current at  $\beta = 1.82$  was presented in Ref. [12].

current	local		conserved	
	$\beta$	2.00	1.82	2.00
$f_+(0)$	0.9602(13)	0.9603(16)	0.9700(13)	0.9740(16)
$L_9 [10^{-3}]$	3.873(37)	3.924(57)	3.585(36)	3.539(58)
$L_5 [10^{-4}]$	7.60(16)	6.94(28)	7.80(15)	7.32(29)
$c_2^+ [\text{GeV}^{-4}]$	1.59(10)	1.19(17)	1.48(10)	1.01(17)
$c_2^0 [\text{GeV}^{-4}]$	-0.152(96)	-0.40(11)	-0.114(96)	-0.36(11)
$c_0$	-0.0068(13)	-0.0077(16)	0.0029(13)	0.0061(16)
$\chi^2/\text{dof}$	0.05	0.05	0.05	0.05

TABLE IX. Results for  $f_+(0)$ ,  $\lambda'_s$ , and  $\lambda''_s$  for  $s = +, 0$  at the physical point at each  $\beta$ , evaluated from the fit results shown in Table VIII.

current	local		conserved	
	$\beta$	2.00	1.82	2.00
$f_+(0)$	0.9617(13)	0.9609(16)	0.9715(13)	0.9746(16)
$\lambda'_+ [10^{-2}]$	2.579(22)	2.614(37)	2.369(22)	2.332(37)
$\lambda'_0 [10^{-2}]$	1.456(20)	1.371(37)	1.467(20)	1.401(37)
$\lambda''_+ [10^{-3}]$	1.376(80)	1.06(13)	1.273(79)	0.91(13)
$\lambda''_0 [10^{-3}]$	0.588(76)	0.394(91)	0.612(75)	0.417(89)

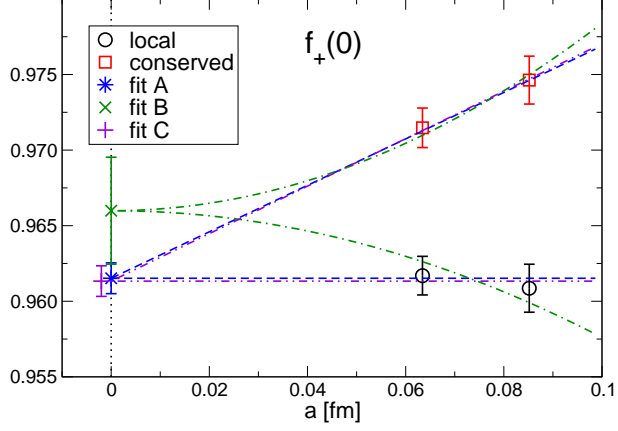


FIG. 12. Lattice spacing dependence of  $f_+(0)$ , whose values are evaluated from a fit result at each lattice spacing using the local (circle) and conserved (square) vector current data. As explained in Sec. IV A, fit lines evaluated from continuum extrapolations for fit A, B, C are also presented.

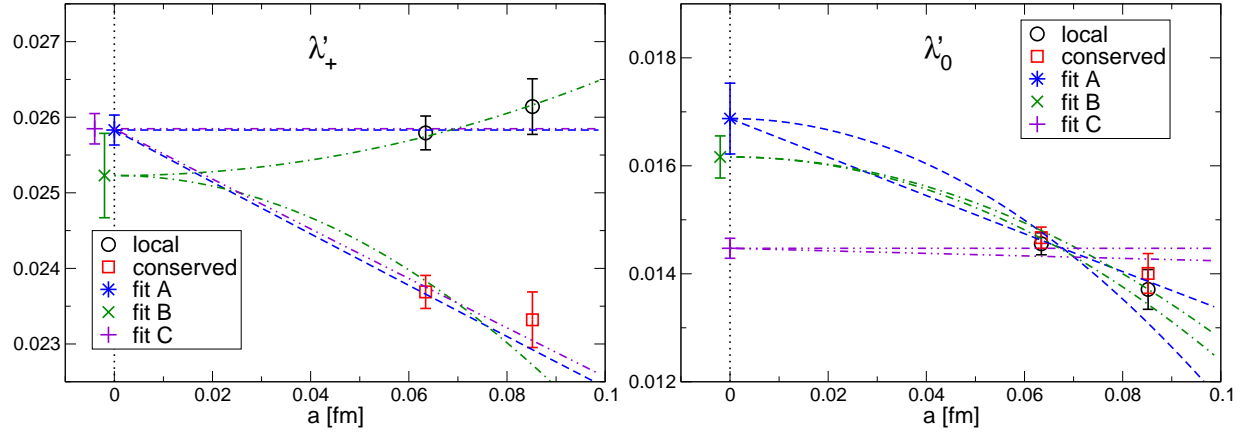


FIG. 13. The same figure as as Fig. 12, but for  $\lambda'_+$  (left) and  $\lambda'_0$  (right).

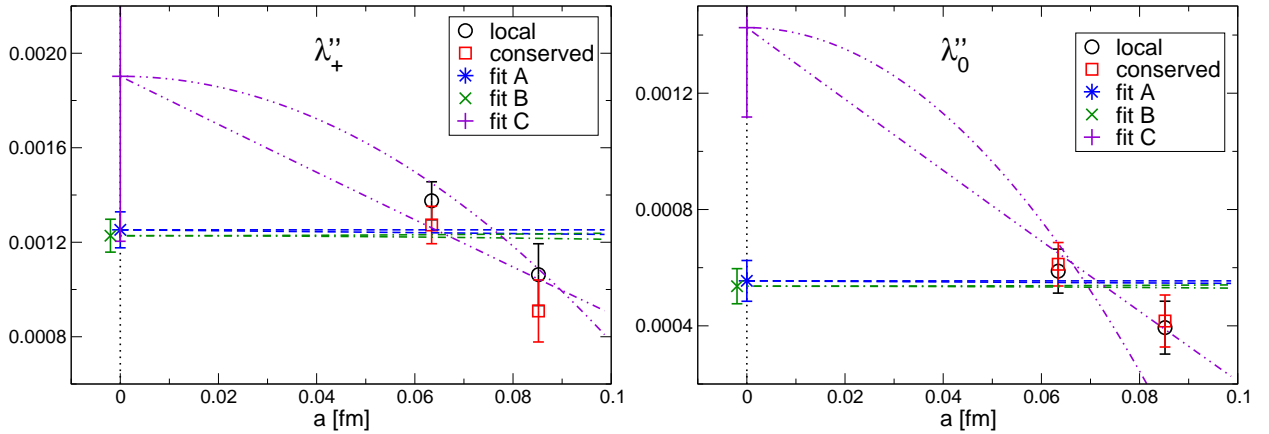


FIG. 14. The same figure as as Fig. 12, but for  $\lambda''_+$  (left) and  $\lambda''_0$  (right).

## IV. RESULT IN THE CONTINUUM LIMIT

In this section continuum extrapolations of the form factors are discussed with the results from the local and conserved vector currents at the two lattice spacings. In our calculation the main result is obtained from the data using the combined and A1 analyses at  $\beta = 2.00$  and 1.82, respectively, whose values are explained in the last section. The data obtained from only the local or smeared operator at  $\beta = 2.00$ , and from the A2 analysis at  $\beta = 1.82$  are used for a systematic error estimation discussed below.

### A. Continuum extrapolation

A continuum extrapolation is carried out using all the data we calculated: the two form factors  $f_+(q^2)$  and  $f_0(q^2)$  with the local and conserved currents at the two lattice spacings. We adopt fit forms based on the NLO SU(3) ChPT formula given in Eqs. (28) and (29), and add further correction terms corresponding to finite lattice spacing effects. As discussed in Sec. III, the effect is different in  $f_+(q^2)$  and  $f_0(q^2)$ , and also in the local and conserved currents. Thus, we introduce functions  $g_+^{\text{cur}}(q^2, a)$  and  $g_0^{\text{cur}}(q^2, a)$  to incorporate the lattice spacing dependence in fit forms given as

$$f_+^{\text{cur}}(q^2) = 1 - \frac{4}{F_0^2} L_9 q^2 + K_+(q^2) + c_0 + c_2^+ q^4 + g_+^{\text{cur}}(q^2, a), \quad (32)$$

$$f_0^{\text{cur}}(q^2) = 1 - \frac{8}{F_0^2} L_5 q^2 + K_0(q^2) + c_0 + c_2^0 q^4 + g_0^{\text{cur}}(q^2, a), \quad (33)$$

where  $\text{cur} = \text{loc}, \text{con}$  correspond to the local and conserved currents, respectively. The same value of  $F_0$  is adopted as in Sec. III C.

From the observations of the finite lattice spacing effects in each form factor discussed in the previous section, we empirically employ the following forms for  $g_{+,0}^{\text{cur}}(q^2, a)$  as,

$$\text{fit A : } g_+^{\text{loc}}(q^2, a) = 0, \quad (34)$$

$$g_0^{\text{loc}}(q^2, a) = d_{21}^0 a^2 q^2, \quad (35)$$

$$g_+^{\text{con}}(q^2, a) = e_{10} a + e_{11}^+ a q^2, \quad (36)$$

$$g_0^{\text{con}}(q^2, a) = e_{10} a + e_{11}^0 a q^2, \quad (37)$$

where  $d_{21}^0, e_{10}, e_{11}^{+,0}$  are free parameters. Our calculation is performed with a nonperturbative  $O(a)$ -improved quark action, while we employ unimproved vector currents in the calculation

of the 3-point functions. It means that  $O(a)$  contributions could appear in our form factor data. We observe that  $f_+(0)$  with the conserved current approximately behaves as a linear function of  $a$  in Fig. 12. In contrast to the conserved current data,  $f_+(0)$  with the local current is reasonably flat as shown in the same figure. Furthermore, the lattice spacing dependence is invisible in  $f_+(q^2)$  as shown in the left panel of Fig 8. From the observations, we assume that  $O(a)$  effects are well suppressed in the local current data. Thus, we choose the above forms for  $g_{+,0}^{\text{loc}}$  and  $g_{+,0}^{\text{con}}$  to explain the lattice spacing dependences for each form factor. Note that  $f_+(0) = f_0(0)$  is satisfied in the fit forms for each current and lattice spacing. We will call this choice of the fit forms as “fit A” in the following. The statistical error of the fit with the different lattice spacing data is estimated by an extension of the jackknife method explained in Appendix B of Ref. [27].

Figure 15 shows that our data for both the form factors are well fitted by the fit A form. The form factors in the continuum limit at the physical point are obtained from the fit result, where the values at the physical point are evaluated in the same way as explained in Sec. III C. The extrapolated results for  $f_+(q^2)$  and  $f_0(q^2)$  in the continuum limit at the physical point are plotted in Fig. 16 with only the statistical error. The values for the fit parameters are given in Table X together with the uncorrelated  $\chi^2/\text{dof}$  value. It should be noted that while we perform uncorrelated fits, the statistical error is properly estimated, because the correlation among the data at the same  $\beta$  is taken into account in the jackknife analysis. This fit gives  $f_+(0) = 0.9615(10)$  in the continuum limit at the physical point, which is well consistent with the results of the local current at each lattice spacing listed in Table IX. The slopes and curvatures for the form factors defined in Eqs. (30) and (31) in the continuum limit are also obtained from the fit result, whose values are summarized in Table X. We choose this fit result as our main result in this study.

A more general choice of  $g_{+,0}^{\text{cur}}$  is examined by assuming that finite lattice spacing effects start from  $O(a^2)$  in all the data. The functional forms of  $g_{+,0}^{\text{cur}}$  with the assumption are given by

$$\text{fit B : } g_+^{\text{loc}}(q^2, a) = d_{20}a^2 + d_{21}^+ a^2 q^2, \quad (38)$$

$$g_0^{\text{loc}}(q^2, a) = d_{20}a^2 + d_{21}^0 a^2 q^2, \quad (39)$$

$$g_+^{\text{con}}(q^2, a) = e_{20}a^2 + e_{21}^+ a^2 q^2, \quad (40)$$

$$g_0^{\text{con}}(q^2, a) = e_{20}a^2 + e_{21}^0 a^2 q^2. \quad (41)$$

This choice is called “fit B” in the following. The fit results are presented in Table X. The fit curves in  $q^2 = 0$  at the physical point for the fit A and B are compared in Fig. 12 together with the data obtained from each current. Those fit forms well explain the data, while the result of  $f_+(0) = 0.9660(35)$  in fit B is much higher than that in fit A. This discrepancy will be included in estimation of a systematic error of  $f_+(0)$  discussed later.

The lattice spacing dependences for the slopes and curvatures at the physical point evaluated from the fit A and B are plotted in Figs. 13 and 14. The fit results of the curvatures are flat, because in the above fits, it is assumed that the dominant lattice artifact of the  $q^2$  dependence is proportional to  $q^2$  in all the form factors, except for  $f_+(q^2)$  in the local current of fit A. Thus, we employ another fit form under an assumption that lattice artifact of  $q^4$  is dominant, except for  $f_+(q^2)$  in the conserved current, where a  $q^2$  term is necessary to explain a linear behavior of the slope as shown in the left panel of Fig. 13. This fit form called “fit C” is given by

$$\text{fit C : } g_+^{\text{loc}}(q^2, a) = d_{22}^+ a^2 q^4, \quad (42)$$

$$g_0^{\text{loc}}(q^2, a) = d_{22}^0 a^2 q^4, \quad (43)$$

$$g_+^{\text{con}}(q^2, a) = e_{10} a + e_{11}^+ a q^2 + e_{12}^+ a q^4, \quad (44)$$

$$g_0^{\text{con}}(q^2, a) = e_{10} a + e_{12}^0 a q^4, \quad (45)$$

based on the fit A form. The fit results for  $f_+(0)$  and  $\lambda'_+$  agree with those of fit A as presented in Table X and Figs. 12 and 13. On the other hand, the results for  $\lambda'_0$  and the curvatures largely depend on the choice of the forms of  $g_{+,0}^{\text{cur}}$ . This is because we have only two different lattice spacings, and those data are almost degenerate at each lattice spacing for the three quantities. For more precise determination for the quantities, data at the third lattice spacing are important, and we plan to carry out the calculation.

A reasonable fit can be performed with  $F_0$  being a free parameter in the fit forms Eqs. (32) and (33) without the  $c_0$  term. The fit results with a free  $F_0$  for fit A, B, and C are summarized in Appendix A. While the fit result of  $F_0$  is a little smaller than the fixed value used in the above fits, each result of  $f_+(0)$  agrees with that using the fixed  $F_0$  fit.

We also carry out continuum extrapolations with monopole, quadratic, and  $z$ -parameter expansion [28] fit forms using  $g_{+,0}^{\text{cur}}$  of fit A. Furthermore, analyses using different data from the main analysis are performed: the local and conserved current data at  $\beta = 2.00$  or  $\beta = 1.82$  are replaced by different dataset in a continuum extrapolation. In an analysis, the

data at  $\beta = 2.00$  are replaced by the local or smeared operator data described in Sec. III. A similar analysis is also carried out with the A2 data instead of the A1 data at  $\beta = 1.82$ . For the different data analyses, the NLO SU(3) ChPT fit formulas with fit A are employed using the fixed and free  $F_0$ . Those results for the continuum extrapolations are summarized in Appendix A, and will be used for systematic error estimations discussed below.

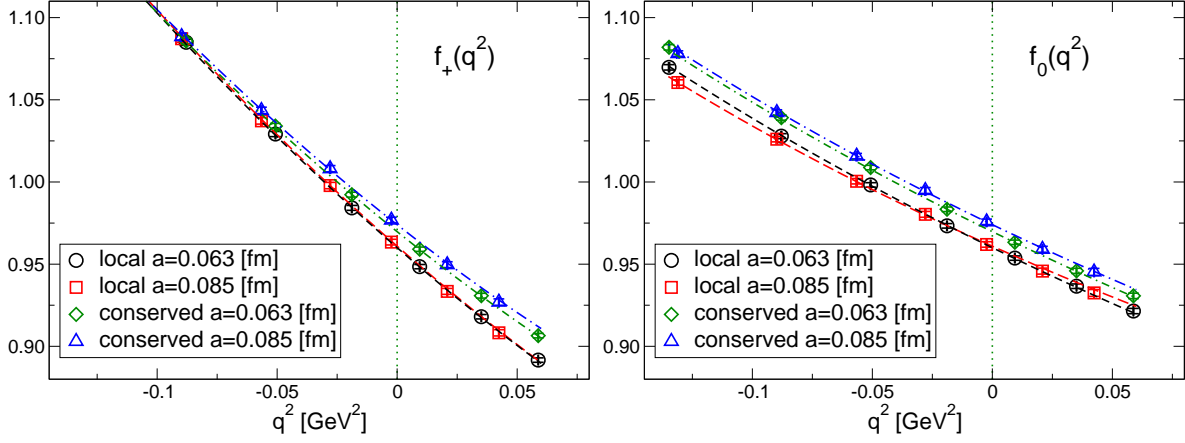


FIG. 15. Fit results of the continuum extrapolation with fit A, defined in Eqs. (32), (33), and (34)–(37), for each data of  $f_+(q^2)$  (left) and  $f_0(q^2)$  (right). The different symbols express different data as explained in the legend.

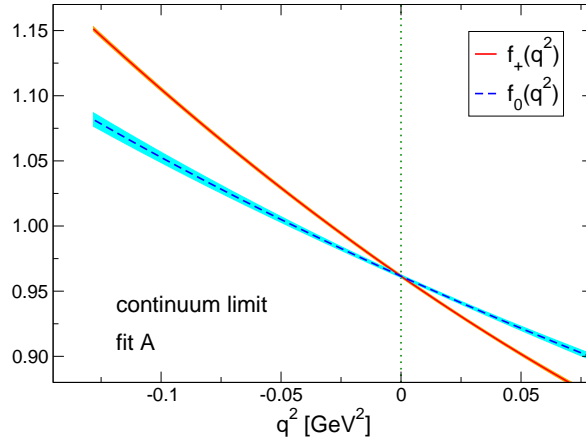


FIG. 16. The results for  $f_+(q^2)$  and  $f_0(q^2)$  in the continuum limit and physical point obtained from fit A. The solid and dashed curves denote  $f_+(q^2)$  and  $f_0(q^2)$ , respectively. Their bands correspond to the statistical errors.

TABLE X. Fit results of the continuum extrapolation of  $K_{\ell 3}$  form factors based on the NLO SU(3) ChPT formulas in Eqs. (32) and (33). The coefficients  $d_{nm}^s$  and  $e_{nm}^s$  of  $a^n q^{2m}$  terms for  $s = +, 0$  in  $g_s^{\text{cur}}$  are defined in text. The values for  $f_+(0)$ ,  $\lambda'_s$ , and  $\lambda''_s$  in the continuum limit at the physical point are also presented together with the value of the uncorrelated  $\chi^2/\text{dof}$ .  $F_0$  is fixed in all the fits.

	fit A	fit B	fit C
$L_9$ [ $10^{-3}$ ]	3.878(32)	3.803(90)	3.880(32)
$L_5$ [ $10^{-4}$ ]	9.39(51)	8.90(30)	7.53(14)
$c_2^+$ [ $\text{GeV}^{-4}$ ]	1.435(96)	1.410(88)	2.26(88)
$c_2^0$ [ $\text{GeV}^{-4}$ ]	-0.194(89)	-0.215(77)	0.91(39)
$c_0$	-0.0070(10)	-0.0025(35)	-0.0072(10)
$\chi^2/\text{dof}$	0.29	0.35	0.26
$d_{20}$ [ $\text{GeV}^2$ ]	...	-0.033(25)	...
$d_{21}^+$	...	-0.020(20)	...
$d_{21}^0$	1.00(27)	0.75(15)	...
$d_{22}^+$ [ $\text{GeV}^{-2}$ ]	...	...	-5.5(6.6)
$d_{22}^0$ [ $\text{GeV}^{-2}$ ]	...	...	-9.1(2.6)
$e_{10}$ [ $\text{GeV}$ ]	0.03032(81)	...	0.03099(80)
$e_{11}^+$ [ $\text{GeV}^{-1}$ ]	0.2965(68)	...	0.284(12)
$e_{11}^0$ [ $\text{GeV}^{-1}$ ]	0.32(10)	...	...
$e_{12}^+$ [ $\text{GeV}^{-3}$ ]	...	...	-2.5(2.3)
$e_{12}^0$ [ $\text{GeV}^{-3}$ ]	...	...	-3.0(1.0)
$e_{20}$ [ $\text{GeV}^2$ ]	...	0.048(25)	...
$e_{21}^+$	...	0.61(20)	...
$e_{21}^0$	...	0.62(15)	...
$f_+(0)$	0.9615(10)	0.9660(35)	0.9613(10)
$\lambda'_+$ [ $10^{-2}$ ]	2.583(20)	2.523(56)	2.585(20)
$\lambda'_0$ [ $10^{-2}$ ]	1.687(66)	1.616(39)	1.447(19)
$\lambda''_+$ [ $10^{-3}$ ]	1.253(76)	1.228(60)	1.90(70)
$\lambda''_0$ [ $10^{-3}$ ]	0.555(70)	0.536(60)	1.43(31)

## B. Result of $f_+(0)$

Our main result of  $f_+(0)$  explained in the last subsection is compared with results from several analyses presented in the above and also Appendix A. Figure 17 presents the comparison, where we plot the results obtained from only the fixed  $F_0$  analyses in the NLO SU(3) ChPT fits denoted by fit A, B, C, local, smear, and A2. The latter three analyses, which are presented in the (2) region of the figure, employ the fit A form as explained above. For the comparison, we also carry out the same analysis as the main result (fit A), but with a narrower  $q^2$  fit range of  $-0.03 \text{ GeV}^2 < q^2 < 0.04 \text{ GeV}^2$  in the continuum extrapolation. Furthermore, continuum extrapolations using only  $f_+(q^2)$  or  $f_0(q^2)$  data are performed to study a stability of our result. All the analyses are consistent with each other, except for the one from fit B with the larger error. This discrepancy is caused by the choice of the fit form for the finite lattice spacing effects as explained in the last subsection. Note that if we employ fit B instead of fit A in the analyses using the different fit forms for  $q^2$  interpolations and different dataset, which are plotted in the (2) and (3) regions in Fig. 17, similar results are obtained to the fit B result in the (1) region. Thus, we include the fit B result in the estimate of the systematic error.

A systematic error of  $f_+(0)$  stemming from the choice of the fit forms and data is estimated by the maximum difference of the central values among our main result and others. Another systematic error from the isospin symmetry breaking effect is also evaluated by the same analysis as in Ref. [12]. In the evaluation the NLO ChPT functions  $K_+$  and  $K_0$  in Eqs. (32) and (33) are replaced by the ones for  $f_+^{K^0\pi^-}$  and  $f_0^{K^0\pi^-}$  in the NLO ChPT with the isospin breaking [21, 29]<sup>3</sup>. The functions with the fit results from the main analysis give  $f_+^{K^0\pi^-}(0) = 0.96106$  in the continuum limit at the physical point. The deviation from our main result is quoted as the systematic error, although it is much smaller than the other systematic error. This effect should be estimated by a nonperturbative calculation as in the  $K_{\ell 2}$  decay [30], but we leave it for future work.

The physical volume in our calculation is more than  $(10 \text{ fm})^3$  at both the lattice spacings, so that the systematic error from the finite volume effect is considered to be negligible. A naive estimation of the effect,  $e^{-m_\pi L}$ , gives 0.08%. Since it is much smaller than our statistical error of  $f_+(0)$ , we neglect the systematic error in this calculation.

<sup>3</sup> The  $\pi$ - $\eta$  mixing parameter  $\epsilon = \sqrt{3}/(4R) = 0.01206$  is employed, which is calculated with the value of  $R = 35.9(1.7)$  in the FLAG review [3].



From the above analyses, our result of  $f_+(0)$  in this study is given by

$$f_+(0) = 0.9615(10)^{(+47)}_{(-3)}(5), \quad (46)$$

where the central value and statistical error (the first error) are determined from the main analysis with fit A. The second and third errors are the systematic errors from the fit forms and isospin breaking effect, respectively. Figure 18 shows a comparison of our result with those obtained in previous lattice calculations in  $N_f = 2$  [31, 32], 2+1 [4–8] including our previous work [12], and 2+1+1 QCD [9–11]. Our result in this work has smaller statistical and systematic errors than the ones of our previous work [12], which used a part of data in this calculation. Especially, the lower systematic error is much reduced.

Due to our large upper systematic error, our result is reasonably consistent with the ones from other groups within  $1.6 \sigma$  in the total error, where the statistical and systematic errors are added in quadrature. The largest discrepancy comes from the result in Ref. [11]. As discussed in our previous work [12], reasons of the discrepancy are not clear at present. There are several differences between the two calculations. The calculation in Ref. [11] employed the HISQ action, and chiral and continuum extrapolations with data in  $m_\pi < 0.3$  GeV using five different lattice spacings on the volumes of  $m_\pi L > 3.2$  in  $N_f = 2 + 1 + 1$  QCD. The finite volume effect is corrected with NLO ChPT. On the other hand, our calculation is performed with a nonperturbatively improved Wilson quark action at the physical point on the larger volumes than  $(10 \text{ fm})^3$  in  $N_f = 2 + 1$  QCD, but we have only two different lattice spacings. If our large systematic error would be significantly reduced and the central value is not changed, serious investigations of the discrepancy will be necessary. To decrease the systematic error for the continuum extrapolation, we plan to repeat the calculation with another set of the PACS10 configuration at a finer lattice spacing.

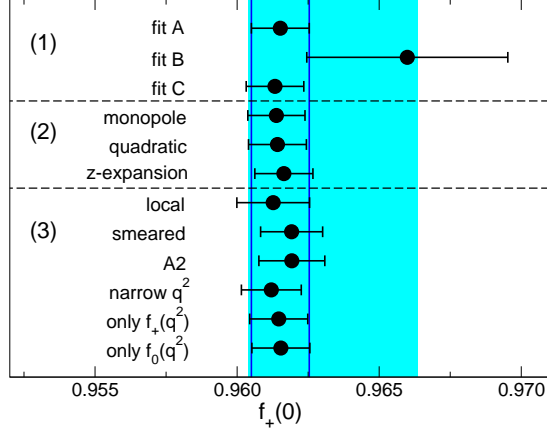


FIG. 17. Comparison of various fit results of  $f_+(0)$ . The vertical solid lines express the statistical error of fit A as our main result. The light blue band represents a systematic error corresponding to difference of fit results. The (1), (2), and (3) regions express analyses using different fit forms for continuum extrapolations, different fit forms for  $q^2$  interpolations, and different dataset, respectively. The analyses in the (2) and (3) regions employ the fit A form for the continuum extrapolation. All the analyses are described in Sec. IV A, except for the last three, which are explained in Sec. IV B.

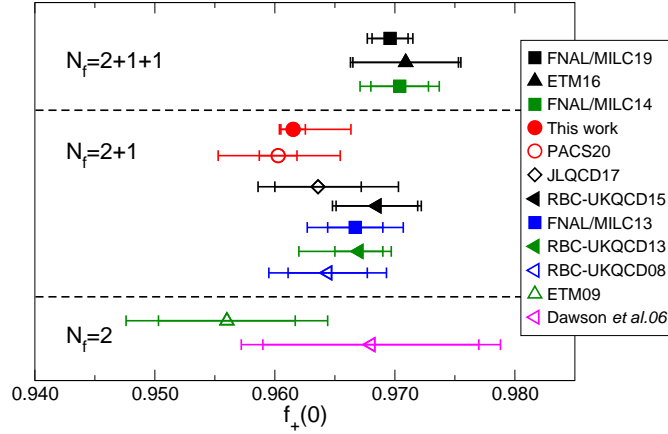


FIG. 18. Comparison of  $f_+(0)$  obtained from this work with previous lattice QCD results in  $N_f = 2$  [31, 32],  $N_f = 2 + 1$  [4–8] including our previous work [12], and  $N_f = 2 + 1 + 1$  [9–11]. The closed and open symbols express results in the continuum limit and at a finite lattice spacing, respectively. The inner and outer errors express the statistical and total errors. The total error is evaluated by adding the statistical and systematic errors in quadrature.

### C. Shape of form factors

A comparison of the results of the slope for the form factors,  $\lambda'_+$  and  $\lambda'_0$  defined in Eq. (30), is presented in Fig. 19. The format of the plot is the same as Fig. 17, but some analyses are not included in the comparison, *e.g.*, the one from the narrower  $q^2$  fit range analysis. In both slopes, the choice of the fit form for the lattice spacing dependence causes the largest discrepancy from our main result (fit A). The central value and statistical error for the slopes are determined from the fit A result. The systematic errors are evaluated in the same way as in those of  $f_+(0)$  explained in the last subsection. Our results for the slopes are given as

$$\lambda'_+ = 0.02583(20)_{(-60)}^{(+39)}(9), \quad (47)$$

$$\lambda'_0 = 0.0169(7)_{(-24)}^{(+11)}(2). \quad (48)$$

The meanings of the second and third errors are the same as  $f_+(0)$  in Eq. (46).

Our results for the slopes are compared with previous lattice QCD results [8, 10, 32] including our calculation [12] in Fig. 20. Both the slopes are reasonably consistent with the previous results and also the experimental values [2],  $\lambda'_+ = 0.02575(36)$  and  $\lambda'_0 = 0.01355(71)^4$ . Since the lattice spacing dependence of  $\lambda'_+$  is well constrained in the continuum extrapolations, its total uncertainty is smaller than our previous result, and comparable to the experimental one. On the other hand, the total error of  $\lambda'_0$  is larger than our previous result, because the lattice spacing dependence is not constrained in our data as presented in the right panel of Fig. 13.

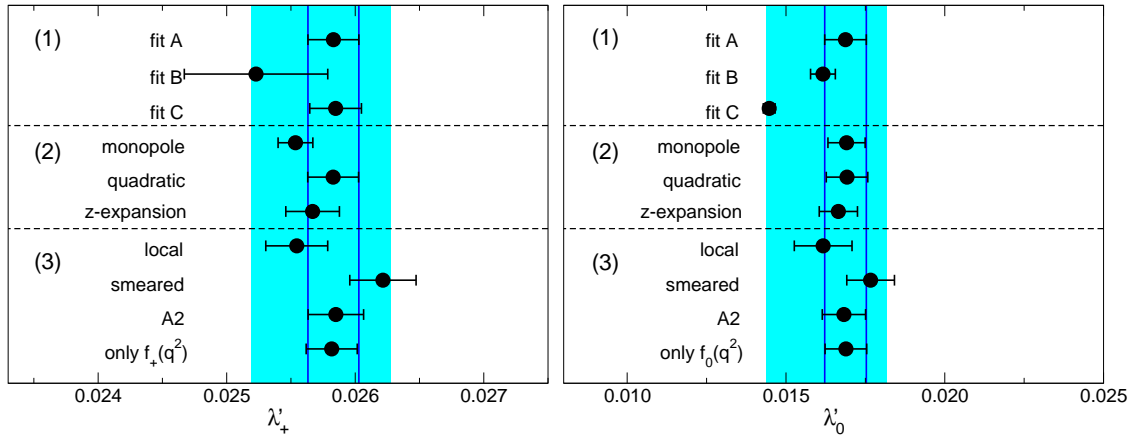


FIG. 19. The same figure as Fig. 17, but for  $\lambda'_+$  (left) and  $\lambda'_0$  (right).

<sup>4</sup> We employ  $\lambda'_0 = m_{\pi^-}^2 / (m_{K^0}^2 - m_{\pi^-}^2) (\log C - 0.0398(44))$  [33] with  $\log C = 0.1985(70)$ .

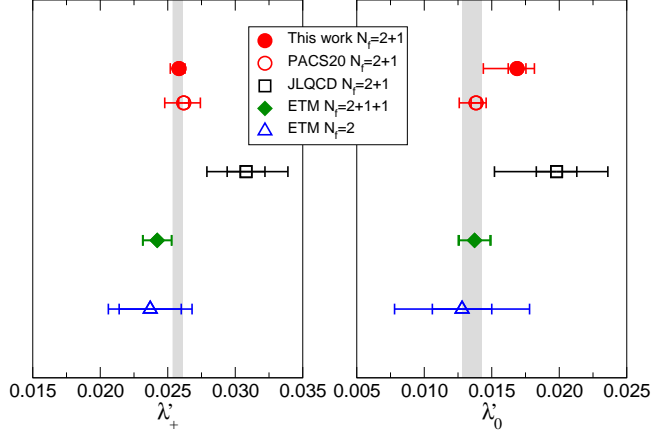


FIG. 20. Comparison of our result for  $\lambda'_+$  (left) and  $\lambda'_0$  (right) with previous lattice QCD results [8, 10, 32] including our previous work [12] and the experimental values [2]. The different symbols denote different lattice QCD results, and the gray band represents the experimental value with one standard deviation. The closed and open symbols express results in the continuum limit and at a finite lattice spacing, respectively. The inner and outer errors express the statistical and total errors. The total error is evaluated by adding the statistical and systematic errors in quadrature.

The same comparison is shown in Fig. 21 for the curvatures,  $\lambda''_+$  and  $\lambda''_0$  defined in Eq. (31). The largest difference from the fit A result is given by fit C in both the cases. The reason is the same as  $\lambda'_0$  due to the unconstrained lattice spacing dependence in our data. Using the same strategy of the estimation of the systematic errors as in the slopes, we obtain the following results for the curvatures as

$$\lambda''_+ = 0.00125(8)^{(+72)}_{(-12)}(0), \quad (49)$$

$$\lambda''_0 = 0.00055(7)^{(+95)}_{(-11)}(1). \quad (50)$$

Figure 22 shows that these values reasonably agree with our previous result [12], the average of the experimental results,  $\lambda''_+ = 0.00157(48)$  [34], and the experimental ones evaluated with the dispersive representation [33]. The larger total errors in our calculation than those in our previous work come from the systematic error of the choice of the fit forms in the continuum extrapolation.

Regarding the large systematic errors in the slopes and curvatures, if the third data at a smaller lattice spacing are calculated, these errors associated with the finite lattice spacing effect can be significantly reduced. Thus, it is an important future work in our calculation.

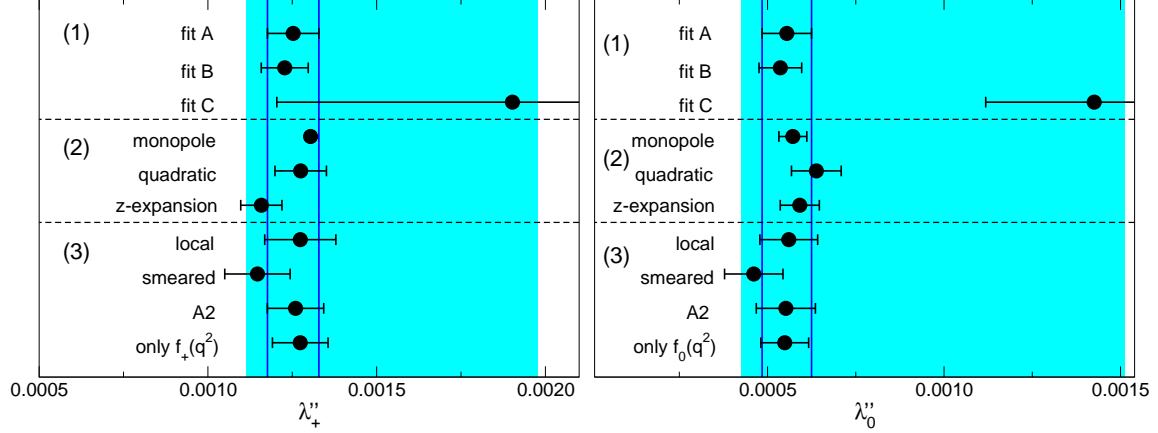


FIG. 21. The same figure as Fig. 17, but for  $\lambda''_+$  (left) and  $\lambda''_0$  (right).

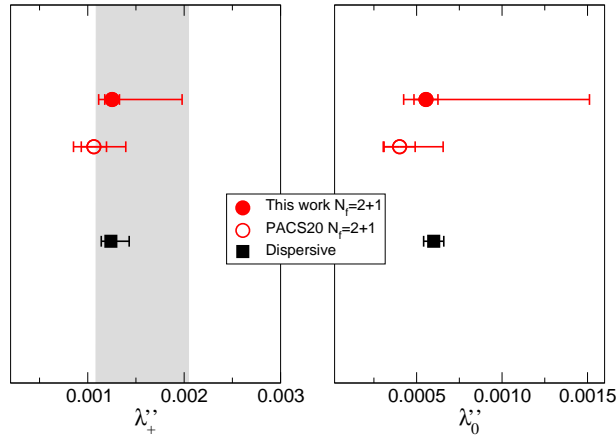


FIG. 22. Comparison of our result for  $\lambda''_+$  (left) and  $\lambda''_0$  (right) with our previous work [12] and experimental values. The square symbol is the experimental value evaluated with the dispersive representation [33], and the gray band represents the average of the experimental results [34] with one standard deviation. The inner and outer errors of the circles express the statistical and total errors. The total error is evaluated by adding the statistical and systematic errors in quadrature.

## D. Phase space integral

The phase space factor  $I_K^\ell$  in Eq. (2) is determined from an integral of the  $q^2$  dependent form factors in a certain  $q^2$  region,  $m_\ell^2 \leq t \leq t_{\max}$ , where  $t = -q^2$ ,  $t_{\max} = (M_K - M_\pi)^2$ , and  $m_\ell$  is the mass of the lepton  $\ell$ ,  $m_e = 0.000511$  GeV, and  $m_\mu = 0.10566$  GeV. Since the  $q^2$  dependence of the form factors is obtained in our calculation, the phase space integral can be calculated using our result in the continuum limit. The phase space integral [35] is defined by

$$I_K^\ell = \int_{m_\ell^2}^{t_{\max}} dt \frac{\lambda^{3/2}}{M_K^8} \left(1 + \frac{m_\ell^2}{2t}\right) \left(1 - \frac{m_\ell^2}{t}\right)^2 \left(\overline{F}_+^2(t) + \frac{3m_\ell^2 \Delta_{K\pi}^2}{(2t + m_\ell^2)\lambda} \overline{F}_0^2(t)\right), \quad (51)$$

where  $\lambda = (t - (M_K + M_\pi)^2)(t - t_{\max})$ ,  $\Delta_{K\pi} = M_K^2 - M_\pi^2$ ,  $\overline{F}_s(t) = f_s(-t)/f_+(0)$  with  $s = +$  and  $0$ . For  $I_{K^0}^\ell$  related to the  $K^0 \rightarrow \pi^- \ell^+ \nu_\ell$  process, we employ  $M_K = m_{K^0} = 0.497611$  GeV and  $M_\pi = m_{\pi^-} = 0.13957061$  GeV. In the calculation of  $I_{K^+}^\ell$  for the  $K^+ \rightarrow \pi^0 \ell^+ \nu_\ell$  process,  $M_K = m_{K^+} = 0.493677$  GeV and  $M_\pi = m_{\pi^0} = 0.1349770$  GeV are used.

The four values of  $I_K^\ell$  obtained from the fit results for the fit A, B, C are tabulated in Table XI. Using the results in the table and those from other fits shown in Appendix A, systematic errors are estimated in the same way as in  $f_+(0)$ . In the four results, the systematic error of the isospin breaking effect is estimated using the NLO ChPT functions for  $f_s^{K^0\pi^-}$  [21, 29] with  $s = +, 0$ , even in  $I_{K^+}^\ell$ . In contrast to this evaluation of the phase space integrals, a correction related to the difference between  $f_+^{K^0\pi^-}$  and  $f_+^{K^+\pi^0}$  is incorporated in the determination of  $|V_{us}|$  from the phase space integrals discussed later. From the estimations, we obtain results for  $I_K^\ell$  as,

$$I_{K^0}^e = 0.15477(7)_{(-33)}^{(+55)}(5), \quad (52)$$

$$I_{K^0}^\mu = 0.1032(2)_{(-20)}^{(+3)}(1), \quad (53)$$

$$I_{K^+}^e = 0.15919(8)_{(-34)}^{(+58)}(1), \quad (54)$$

$$I_{K^+}^\mu = 0.1063(2)_{(-21)}^{(+3)}(0). \quad (55)$$

These results agree well with the experimental values in the dispersive representation of the form factors,  $I_{K^0}^e = 0.15476(18)$ ,  $I_{K^0}^\mu = 0.10253(16)$ ,  $I_{K^+}^e = 0.15922(18)$ ,  $I_{K^+}^\mu = 0.10559(17)$ , in Ref. [34], and also their updates,  $I_{K^0}^e = 0.15470(15)$ ,  $I_{K^0}^\mu = 0.10247(15)$ ,  $I_{K^+}^e = 0.15915(15)$ ,  $I_{K^+}^\mu = 0.10553(16)$  in Ref. [36].

In the next subsection, we will determine  $|V_{us}|$  using our results of  $I_K^\ell$ . For the determination, we also evaluate  $f_+(0)\sqrt{I_K^\ell}$  in each process as

$$f_+(0)\sqrt{I_{K^0}^e} = 0.3783(4)({}_{-3}^{+14})(1), \quad (56)$$

$$f_+(0)\sqrt{I_{K^0}^\mu} = 0.3089(5)({}_{-17}^{+6})(0), \quad (57)$$

$$f_+(0)\sqrt{I_{K^+}^e} = 0.3836(4)({}_{-3}^{+15})(2), \quad (58)$$

$$f_+(0)\sqrt{I_{K^+}^\mu} = 0.3135(5)({}_{-17}^{+7})(2). \quad (59)$$

The values obtained from each continuum extrapolation are compiled in Table XI and also summarized in Appendix A.

TABLE XI. Results of phase space integrals in the continuum limit at the physical point obtained from each fit listed in Table X.

	fit A	fit B	fit C
$I_{K^0}^e$	0.154769(75)	0.15444(29)	0.15526(55)
$I_{K^0}^\mu$	0.10319(16)	0.10114(70)	0.10335(49)
$I_{K^+}^e$	0.159186(77)	0.15884(30)	0.15969(56)
$I_{K^+}^\mu$	0.10630(17)	0.10418(72)	0.10646(50)
$f_+(0)\sqrt{I_{K^0}^e}$	0.37827(42)	0.3796(15)	0.37879(83)
$f_+(0)\sqrt{I_{K^0}^\mu}$	0.30887(45)	0.3072(14)	0.30905(84)
$f_+(0)\sqrt{I_{K^+}^e}$	0.38363(43)	0.3850(15)	0.38416(85)
$f_+(0)\sqrt{I_{K^+}^\mu}$	0.31349(46)	0.3118(14)	0.31367(86)

### E. Result of $|V_{us}|$

Combining our result of  $f_+(0)$  in Eq. (46) and the experimental value,  $f_+(0)|V_{us}| = 0.21654(41)$  [2], we determine the value of  $|V_{us}|$  as

$$|V_{us}| = 0.22521(24)({}_{-109}^{+6})(11)(43). \quad (60)$$

The statistical (first) and systematical (second and third) errors correspond to those in  $f_+(0)$ . The additional fourth error from the experimental value. When an updated

value of  $f_+(0)|V_{us}| = 0.21635(39)$  [36] is employed, the obtained value is not largely changed as  $|V_{us}| = 0.22501(24)_{(-109)}^{(+6)}(11)(41)$ .

In Fig. 23, our value of  $|V_{us}|$  is compared with several previous results using  $f_+(0)$  in the  $N_f = 2 + 1$  and  $2+1+1$  lattice QCD calculations [4, 7, 8, 10, 11] including our previous work [12]. The inner error originates from the lattice calculation. On the other hand, the outer error corresponds to the total error, where the errors in the lattice QCD calculation and experimental value are added in quadrature. Similar to the comparison of  $f_+(0)$ , our result is reasonably consistent with other lattice results, while our central value is a little larger than most of all results. The largest discrepancy, however, is only  $1.4 \sigma$ , so that it is not so significant in the current total error.

Our result also agrees with the value in PDG20 [1] determined through the  $K_{\ell 2}$  processes, and the one using our results of  $F_K/F_\pi$  calculated with the PACS10 configurations at  $\beta = 2.00$  and  $1.82$ ,  $|V_{us}| = 0.22486(32)_{(-0)}^{(+60)}(30)$ , as plotted in Fig. 23. Our central value and statistical (first) error are determined from the result of  $\beta = 2.00$ , and the asymmetric systematic (second) error is estimated from the difference between the results at the two lattice spacings. The third error stems from the experimental values,  $|V_{us}|F_K/|V_{ud}|F_\pi = 0.27599(37)$  [2] and  $|V_{ud}| = 0.97370(14)$  [37]. If an updated value of  $|V_{us}|F_K/|V_{ud}|F_\pi = 0.27683(35)$  [30] is used in the determination,  $|V_{us}|$  is shifted to a little larger value within the total uncertainty.

The value of  $|V_{us}|$  is evaluated from the unitarity of the first row of the CKM matrix,  $|V_{us}| \approx \sqrt{1 - |V_{ud}|^2} = 0.2278(6)$  under the assumption  $|V_{ub}| \ll 1$ , whose value with one standard deviation is shown by the light blue band in Fig. 23. This value differs from our  $K_{\ell 3}$  result by  $3.4 \sigma$ . We would need more precise studies of systematic errors in lattice calculations and also  $|V_{ud}|$  [38] to conclude whether the difference suggests a signal of new physics or not. The reason is that another determination of  $|V_{ud}| = 0.97373(31)$  [38] with a larger error gives  $|V_{us}| = 0.2277(13)$  through the unitarity, as expressed by the gray band in the figure, whose discrepancy from our result is  $1.8 \sigma$ .

Using our results of the phase space integrals in Eqs. (56)–(59),  $|V_{us}|$  is determined through six kaon decay processes as presented in Table XII. For each decay process, the experimental value of  $|V_{us}|f_+(0)\sqrt{I_K^\ell}$  is also tabulated in the table, which is obtained using the experimental inputs and correction factors [34, 36, 39–41] including the correction of the



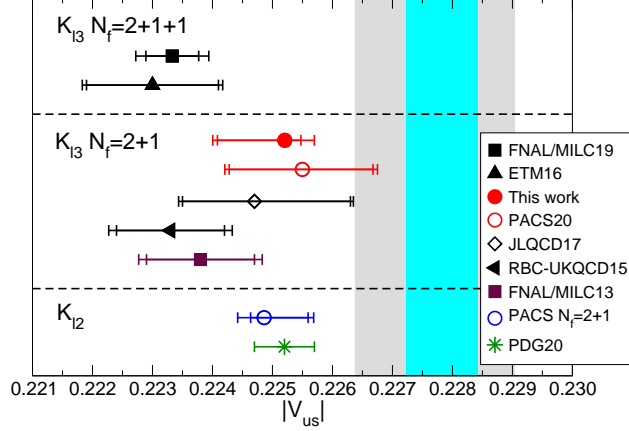


FIG. 23. Comparison of  $|V_{us}|$  in this work with previous lattice QCD results obtained from the  $K_{\ell 3}$  form factor [6–8, 10, 11] including our previous work [12].  $|V_{us}|$  determined from the  $K_{\ell 2}$  decay are also plotted using  $F_K/F_\pi$  in our calculation and PDG20 [1]. The inner and outer errors express the error of the lattice calculation and total error. The total error is evaluated by adding the lattice QCD and experimental errors in quadrature. The closed and open symbols express results in the continuum limit and at a finite lattice spacing, respectively. The unitarity values using  $|V_{ud}|$  in Refs. [37] and [38] are presented by the light blue and gray bands, respectively.

TABLE XII. Results of  $|V_{us}|$  obtained from our results of the phase space integrals in Eqs. (56)–(59). The errors of  $|V_{us}|$  are explained in text. The inputs for each decay process,  $|V_{us}|f_+(0)\sqrt{I_K^\ell}$ , are also tabulated.

	$ V_{us} $	$ V_{us} f_+(0)\sqrt{I_K^\ell}$
$K_L e$	$0.22480(25)_{(-86)}^{(+16)}(7)(53)$	$0.08503(20)$
$K_L \mu$	$0.22439(33)_{(-45)}^{(+121)}(2)(62)$	$0.06931(19)$
$K_S e$	$0.22386(25)_{(-85)}^{(+16)}(7)(127)$	$0.08468(48)$
$K_S \mu$	$0.22026(32)_{(-44)}^{(+119)}(2)(483)$	$0.06803(149)$
$K^+ e$	$0.22581(25)_{(-86)}^{(+16)}(10)(94)$	$0.08663(36)$
$K^+ \mu$	$0.22486(33)_{(-47)}^{(+122)}(13)(114)$	$0.07049(36)$

difference of  $f_+^{K^0\pi^-}(0)$  and  $f_+^{K^+\pi^0}(0)$ . A weighted average of the six processes gives

$$|V_{us}| = 0.22469(27)_{(-77)}^{(+39)}(6)(40). \quad (61)$$

The results for the six processes and also a weighted average are well consistent with the

one determined from  $f_+(0)$  in Eq. (60).

## V. CONCLUSIONS

We have updated our calculation of the  $K_{\ell 3}$  form factors on a more than  $(10 \text{ fm})^3$  volume at the physical point by adding the result at the second lattice spacing of 0.063 fm. The calculation is performed using the local and conserved vector currents. We have observed that lattice spacing dependences in the  $f_+(0)$  data for the two vector currents are clearly different.

Using the data of the form factors at the two different lattice spacings, continuum extrapolation and  $q^2$  interpolation are carried out simultaneously using fit forms based on the NLO SU(3) ChPT. The obtained result of  $f_+(0)$  is stable against several fit forms of  $q^2$ , while it largely depends on fitting function of the lattice spacing. This is because it is hard to constrain fit forms of the lattice spacing dependence using our data at only two lattice spacings. Similar trends of the fitting function dependence for the lattice spacing effect are observed in the results for the slope and curvature of the form factors. Our final results are summarized as follows:

$$f_+(0) = 0.9615(10) \binom{+47}{-3}(5), \quad (62)$$

$$\lambda'_+ = 0.02583(20) \binom{+39}{-60}(9), \quad (63)$$

$$\lambda'_0 = 0.0169(7) \binom{+11}{-24}(2), \quad (64)$$

$$\lambda''_+ = 0.00125(8) \binom{+72}{-12}(0), \quad (65)$$

$$\lambda''_0 = 0.00055(7) \binom{+95}{-11}(1). \quad (66)$$

The first error is the statistical, the second one is the systematic error involving the fit form and data dependences, and the last one represents the systematic error from the isospin breaking effect, respectively. As described above, the second error is the largest in our result.

Our  $f_+(0)$  is reasonably consistent with recent lattice QCD results. The relative difference from the most precise result is not so significant,  $1.6 \sigma$ , at present due to our large systematic error. If our systematic error is largely decreased in a similar central value, we would need detailed investigations for the difference. For the slopes and curvatures, our results are in good agreement with other lattice results and the experimental values, while our systematic

errors are much larger than those in the experiment, except for  $\lambda'_+$ , which has a comparable error to the experiment.

Using our  $f_+(0)$  and the experimental input, we have obtained the value of  $|V_{us}|$  as

$$|V_{us}| = 0.22521(24)(_{-109}^{+6})(11)(43). \quad (67)$$

The errors from the first to the third correspond to the same ones as in the above  $f_+(0)$ . The fourth error comes from the experimental input. This value can be expressed by  $|V_{us}| = 0.2252(_{-12}^{+5})$ . Our result is reasonably consistent with those using the recent lattice results of  $f_+(0)$ , and also well agrees with the values of  $|V_{us}|$  determined through the  $K_{\ell 2}$  decay. On the other hand, we have observed a discrepancy from that of the unitarity of the first row of the CKM matrix. Its significance, however, depends on the size of error of  $|V_{ud}|$ . For the BSM search through  $|V_{us}|$ , it would be important to decrease the uncertainties in both the lattice QCD and  $|V_{ud}|$  in future.

We have also computed the phase space integrals from our  $q^2$  dependent form factors as,

$$I_{K^0}^e = 0.15477(7)(_{-33}^{+55})(5), \quad (68)$$

$$I_{K^0}^\mu = 0.1032(2)(_{-20}^{+3})(1), \quad (69)$$

$$I_{K^+}^e = 0.15919(8)(_{-34}^{+58})(1), \quad (70)$$

$$I_{K^+}^\mu = 0.1063(2)(_{-21}^{+3})(0). \quad (71)$$

Those results are well consistent with the experimental values in the dispersive representation of the form factors. Using our results for the phase space integrals, the experimental inputs, and the correction factors, the values of  $|V_{us}|$  are determined through six  $K_{\ell 3}$  decay processes. An average of the six decay processes given as,

$$|V_{us}| = 0.22469(27)(_{-77}^{+39})(6)(40), \quad (72)$$

well agrees with that in the above with  $f_+(0)$ . This agreement insists that the form factors calculated in the lattice QCD are useful for the evaluation of the phase space integrals as well as for the determination of  $f_+(0)$ .

While in this work the lower uncertainty of our  $f_+(0)$  is much smaller than that in our previous work, the upper one is still similar in size. An additional data at a smaller lattice spacing could largely reduce the uncertainty, because our main systematic error comes from the choice of the fitting forms of the lattice spacing dependence in the continuum

extrapolation. This is an important future direction of our calculation, and we are generating the PACS10 configuration at the third lattice spacing. Furthermore, the isospin breaking effect of the form factors is estimated with the NLO SU(3) ChPT formulas in this work, while this effect can be evaluated using a lattice calculation. It is also an important future work for the indirect search for a BSM physics.

## ACKNOWLEDGMENTS

Numerical calculations in this work were performed on Oakforest-PACS in Joint Center for Advanced High Performance Computing (JCAHPC) under Multidisciplinary Cooperative Research Program of Center for Computational Sciences, University of Tsukuba. This research also used computational resources of Oakforest-PACS by Information Technology Center of the University of Tokyo, and of Fugaku by RIKEN CCS through the HPCI System Research Project (Project ID: hp170022, hp180051, hp180072, hp180126, hp190025, hp190081, hp200062, hp200167, hp210112, hp220079). The calculation employed OpenQCD system<sup>5</sup>. This work was supported in part by Grants-in-Aid for Scientific Research from the Ministry of Education, Culture, Sports, Science and Technology (Nos. 18K03638, 19H01892). This work was supported by the JLDG constructed over the SINET5 of NII.

## Appendix A: Results with several fit forms

In this appendix results for continuum extrapolations using various fit forms and different data are summarized. These results are used to estimate systematic errors of our main result as discussed in the main text.

The same continuum extrapolations using the formulas based on the NLO SU(3) ChPT explained in Sec. IV A are performed, but the decay constant  $F_0$  is a free parameter and  $c_0$  is omitted in the fit functions shown in Eqs. (32) and (33). These fit results for the fit A, B, C, whose functional forms are described in Sec. IV A, are summarized in Table XIII. The phase space integral calculated by Eq. (51) for each fit is shown in Table XIV.

We also compare results with a different choice of data. In a continuum extrapolation, the form factor data at  $\beta = 2.00$  are replaced by those obtained from the analysis with

---

<sup>5</sup> <http://luscher.web.cern.ch/luscher/openQCD/>

only the local or smeared operator data, whose values are presented in Table V for the local current and in Table VI for the conserved current in Sec. III. Furthermore, we perform a continuum extrapolation with the replaced data at  $\beta = 1.82$  by the ones obtained from the A2 analysis shown in Table VII for the conserved current in Sec. III and Table II of Ref. [12] for the local current. In all the extrapolations, the fit A form is employed for the lattice spacing dependence. Those fit results and phase space integrals are tabulated in Tables XV and XVI for a fixed  $F_0$ , and Tables XVII and XVIII for a free  $F_0$ .

In order to carry out continuum extrapolations with other fitting forms for a  $q^2$  interpolation, *e.g.*, a monopole form, estimate of the form factors at the physical point is necessary, though effects of the chiral extrapolation are considered to be tiny. We estimate the values of the form factors at the physical point in each lattice spacing by using the  $q^2$  fit results with the NLO SU(3) ChPT formula in each current data and lattice spacing presented in Sec. III C. At each  $q_{np}^2$ , a difference of  $f_s(q^2)$  for  $s = +, 0$  in between the measure meson masses and the physical point,

$$\Delta f_s(q^2) = f_s(q^2)|_{m_{\pi^-}, m_{K^0}} - f_s(q^2)|_{m_{\pi}, m_K}, \quad (\text{A1})$$

is evaluated from the fit results, where  $f_s(q^2)|_{m_{\pi^-}, m_{K^0}}$  is estimated in the same way as explained in Sec. III C. Each data is shifted by adding  $\Delta f_s(q^2)$  to estimate the value at the physical point. The values of the shifted data are tabulated in Tables XIX and XX. The original values of the form factors are summarized in Tables V and VI labeled by “combined”, Table VII, and Table II in Ref. [12] labeled by “A1”. Comparing to those original values, it is found that the shifts are almost the same size as or less than the statistical errors.

Using the shifted data, we perform continuum extrapolations with a monopole form,

$$f_+^{\text{cur}}(q^2) = \frac{f_+(0)}{1 + c_1^+ q^2} + g_+^{\text{cur}}(q^2, a), \quad (\text{A2})$$

$$f_0^{\text{cur}}(q^2) = \frac{f_+(0)}{1 + c_1^0 q^2} + g_0^{\text{cur}}(q^2, a), \quad (\text{A3})$$

a quadratic form,

$$f_+^{\text{cur}}(q^2) = f_+(0) + c_1^+ q^2 + c_2^+ q^4 + g_+^{\text{cur}}(q^2, a), \quad (\text{A4})$$

$$f_0^{\text{cur}}(q^2) = f_+(0) + c_1^0 q^2 + c_2^0 q^4 + g_0^{\text{cur}}(q^2, a), \quad (\text{A5})$$

TABLE XIII. Fit results of the continuum extrapolation of  $K_{\ell 3}$  form factors based on the NLO SU(3) ChPT formulas in Eqs. (28) and (29) together with the value of the uncorrelated  $\chi^2/\text{dof}$ .  $F_0$  is a free parameter in all the fits.

	fit A	fit B	fit C
$L_9 [10^{-3}]$	3.178(96)	3.54(38)	3.164(97)
$L_5 [10^{-4}]$	7.30(55)	8.1(1.1)	5.54(27)
$c_2^+ [\text{GeV}^{-4}]$	1.390(94)	1.395(88)	2.32(88)
$c_2^0 [\text{GeV}^{-4}]$	-0.404(92)	-0.29(13)	0.82(40)
$F_0 [\text{GeV}]$	0.1017(13)	0.1081(52)	0.1015(13)
$\chi^2/\text{dof}$	0.37	0.35	0.32
$d_{20} [\text{GeV}^2]$	...	-0.034(24)	...
$d_{21}^+$	...	-0.20(20)	...
$d_{21}^0$	1.11(27)	0.77(16)	...
$d_{22}^+ [\text{GeV}^{-2}]$	...	...	-6.3(6.6)
$d_{22}^0 [\text{GeV}^{-2}]$	...	...	-10.1(2.6)
$e_{10} [\text{GeV}]$	0.03015(89)	...	0.03084(88)
$e_{11}^+ [\text{GeV}^{-1}]$	0.2972(66)	...	0.285(13)
$e_{11}^0 [\text{GeV}^{-1}]$	0.36(10)	...	...
$e_{12}^+ [\text{GeV}^{-3}]$	...	...	-2.7(2.3)
$e_{12}^0 [\text{GeV}^{-3}]$	...	...	-3.39(95)
$e_{20} [\text{GeV}^2]$	...	0.048(24)	...
$e_{21}^+$	...	0.62(20)	...
$e_{21}^0$	...	0.64(16)	...
$f_+(0)$	0.96184(98)	0.9662(32)	0.96164(98)
$\lambda'_+ [10^{-2}]$	2.584(20)	2.525(55)	2.587(20)
$\lambda'_0 [10^{-2}]$	1.718(66)	1.624(42)	1.451(18)
$\lambda''_+ [10^{-3}]$	1.243(74)	1.224(69)	1.97(69)
$\lambda''_0 [10^{-3}]$	0.540(69)	0.530(60)	1.51(31)

TABLE XIV. Results of phase space integrals in the continuum limit at the physical point obtained from each fit listed in Table XIII.

	fit A	fit B	fit C
$I_{K^0}^e$	0.154766(75)	0.15445(29)	0.15532(54)
$I_{K^0}^\mu$	0.10325(16)	0.10121(73)	0.10344(48)
$I_{K^+}^e$	0.159192(77)	0.15886(30)	0.15977(56)
$I_{K^+}^\mu$	0.10639(17)	0.10426(76)	0.10658(50)
$f_+(0)\sqrt{I_{K^0}^e}$	0.37839(41)	0.3797(13)	0.37899(82)
$f_+(0)\sqrt{I_{K^0}^\mu}$	0.30907(43)	0.3074(12)	0.30928(83)
$f_+(0)\sqrt{I_{K^+}^e}$	0.38376(41)	0.3851(14)	0.38437(83)
$f_+(0)\sqrt{I_{K^+}^\mu}$	0.31372(44)	0.3120(12)	0.31394(84)

and the second order of the  $z$ -parameter expansion [28],

$$f_+^{\text{cur}}(q^2) = f_+(0) + c_1^+ z^2(q^2) + c_2^+ z^4(q^2) + g_+^{\text{cur}}(q^2, a), \quad (\text{A6})$$

$$f_0^{\text{cur}}(q^2) = f_+(0) + c_1^0 z^2(q^2) + c_2^0 z^4(q^2) + g_0^{\text{cur}}(q^2, a), \quad (\text{A7})$$

where

$$z(q^2) = \frac{\sqrt{(m_{K^0} + m_{\pi^-})^2 + q^2} - (m_{K^0} + m_{\pi^-})}{\sqrt{(m_{K^0} + m_{\pi^-})^2 + q^2} + (m_{K^0} + m_{\pi^-})}. \quad (\text{A8})$$

Our choice of  $z(q^2)$  corresponds to the one with  $t_0 = 0$  in the general representation of  $z(q^2)$  [28]. In the three fits, the functional form of  $g_s^{\text{cur}}$  is fixed to the ones in fit A described in Sec. IV A. The fit results are tabulated in Table. XXI together with the results for the slopes and curvatures. The phase space integrals evaluated using the fit results are presented in Table XXII.

TABLE XV. The same table as Table XIII, but for using the local and smeared operator data at  $\beta = 2.00$ , and the A2 analysis data at  $\beta = 1.82$ .  $F_0$  is fixed in all the fits.

	local	smeared	A2
$L_9$ [ $10^{-3}$ ]	3.833(38)	3.940(40)	3.883(35)
$L_5$ [ $10^{-4}$ ]	8.85(71)	10.01(58)	9.36(53)
$c_2^+$ [ $\text{GeV}^{-4}$ ]	1.46(13)	1.30(12)	1.44(11)
$c_2^0$ [ $\text{GeV}^{-4}$ ]	-0.19(10)	-0.31(10)	-0.20(11)
$c_0$	-0.0073(13)	-0.0066(11)	-0.0066(12)
$\chi^2/\text{dof}$	0.26	0.45	0.21
$d_{21}^0$	0.80(33)	1.17(27)	1.01(30)
$e_{10}$ [ $\text{GeV}$ ]	0.03064(91)	0.03032(85)	0.03043(77)
$e_{11}^+$ [ $\text{GeV}^{-1}$ ]	0.2879(63)	0.3103(73)	0.2984(84)
$e_{11}^0$ [ $\text{GeV}^{-1}$ ]	0.25(13)	0.39(10)	0.32(11)
$f_+(0)$	0.9613(13)	0.9619(11)	0.9619(12)
$\lambda'_+$ [ $10^{-2}$ ]	2.545(24)	2.622(26)	2.585(22)
$\lambda'_0$ [ $10^{-2}$ ]	1.617(91)	1.766(75)	1.682(68)
$\lambda''_+$ [ $10^{-3}$ ]	1.27(11)	1.147(97)	1.260(84)
$\lambda''_0$ [ $10^{-3}$ ]	0.560(82)	0.461(83)	0.552(84)

TABLE XVI. The same table as Table XIV, but for each fit result listed in Table XV.

	local	smeared	A2
$I_{K^0}^e$	0.154635(85)	0.154893(87)	0.154784(83)
$I_{K^0}^\mu$	0.10296(22)	0.10340(19)	0.10319(17)
$I_{K^+}^e$	0.159048(88)	0.159314(90)	0.159202(86)
$I_{K^+}^\mu$	0.10606(22)	0.10651(20)	0.10630(18)
$f_+(0)\sqrt{I_{K^0}^e}$	0.37801(51)	0.37858(44)	0.37845(48)
$f_+(0)\sqrt{I_{K^0}^\mu}$	0.30845(56)	0.30931(45)	0.30900(53)
$f_+(0)\sqrt{I_{K^+}^e}$	0.38336(52)	0.38394(44)	0.38381(49)
$f_+(0)\sqrt{I_{K^+}^\mu}$	0.31306(56)	0.31393(46)	0.31362(54)



TABLE XVII. The same table as Table XV, but for fits with a free  $F_0$ .

	local	smeared	A2
$L_9$ [ $10^{-3}$ ]	3.11(11)	3.26(10)	3.22(11)
$L_5$ [ $10^{-4}$ ]	6.78(73)	7.92(60)	7.38(64)
$c_2^+$ [ $\text{GeV}^{-4}$ ]	1.42(13)	1.26(12)	1.40(10)
$c_2^0$ [ $\text{GeV}^{-4}$ ]	-0.41(11)	-0.51(10)	-0.39(11)
$F_0$ [GeV]	0.1014(16)	0.1023(14)	0.1023(15)
$\chi^2/\text{dof}$	0.30	0.55	0.23
$d_{21}^0$	0.90(33)	1.27(28)	1.11(30)
$e_{10}$ [GeV]	0.0305(10)	0.03011(95)	0.03030(84)
$e_{11}^+$ [ $\text{GeV}^{-1}$ ]	0.2884(62)	0.3103(71)	0.2993(82)
$e_{11}^0$ [ $\text{GeV}^{-1}$ ]	0.30(13)	0.43(10)	0.36(11)
$f_+(0)$	0.9615(12)	0.9622(11)	0.9622(11)
$\lambda'_+$ [ $10^{-2}$ ]	2.554(24)	2.622(26)	2.586(22)
$\lambda'_0$ [ $10^{-2}$ ]	1.649(93)	1.796(76)	1.711(67)
$\lambda''_+$ [ $10^{-3}$ ]	1.27(10)	1.136(95)	1.251(82)
$\lambda''_0$ [ $10^{-3}$ ]	0.544(79)	0.445(82)	0.539(82)

TABLE XVIII. The same table as Table XIV, but for each fit result listed in Table XVII.

	local	smeared	A2
$I_{K^0}^e$	0.154630(86)	0.154888(87)	0.154784(84)
$I_{K^0}^\mu$	0.10302(22)	0.10345(19)	0.10325(17)
$I_{K^+}^e$	0.159052(89)	0.159317(90)	0.159211(86)
$I_{K^+}^\mu$	0.10615(22)	0.10659(19)	0.10638(17)
$f_+(0)\sqrt{I_{K^0}^e}$	0.37811(50)	0.37869(42)	0.37857(46)
$f_+(0)\sqrt{I_{K^0}^\mu}$	0.30863(55)	0.30949(43)	0.30919(50)
$f_+(0)\sqrt{I_{K^+}^e}$	0.38348(50)	0.38407(43)	0.38395(47)
$f_+(0)\sqrt{I_{K^+}^\mu}$	0.31328(55)	0.31415(44)	0.31385(51)

TABLE XIX. Form factors  $f_+(q^2)$  and  $f_0(q^2)$  at the physical point in each  $q^2$  at  $\beta = 2.00$  and  $1.82$  using the local vector current for the combined and A1 analyses, respectively.

	$\beta = 2.00$		$\beta = 1.82$	
$q^2$	$f_+(q^2)$	$f_0(q^2)$	$f_+(q^2)$	$f_0(q^2)$
$q_0^2$	...	1.0741(17)	...	1.0602(18)
$q_1^2$	1.0871(19)	1.0312(16)	1.0876(22)	1.0260(17)
$q_2^2$	1.0310(16)	1.0007(14)	1.0377(21)	1.0007(17)
$q_3^2$	0.9859(15)	0.9752(14)	0.9984(20)	0.9807(18)
$q_4^2$	0.9499(13)	0.9550(13)	0.9640(17)	0.9626(17)
$q_5^2$	0.9193(13)	0.9375(13)	0.9340(18)	0.9465(18)
$q_6^2$	0.8928(13)	0.9220(16)	0.9089(19)	0.9333(21)

TABLE XX. The same table as Table XIX, but for the conserved current data.

	$\beta = 2.00$		$\beta = 1.82$	
$q^2$	$f_+(q^2)$	$f_0(q^2)$	$f_+(q^2)$	$f_0(q^2)$
$q_0^2$	...	1.0863(17)	...	1.0778(18)
$q_1^2$	1.0879(19)	1.0424(16)	1.0889(21)	1.0423(17)
$q_2^2$	1.0359(16)	1.0112(14)	1.0440(20)	1.0160(17)
$q_3^2$	0.9939(15)	0.9852(14)	1.0086(20)	0.9953(18)
$q_4^2$	0.9605(13)	0.9646(13)	0.9774(17)	0.9763(17)
$q_5^2$	0.9321(15)	0.9468(16)	0.9503(18)	0.9598(18)
$q_6^2$	0.9076(14)	0.9312(16)	0.9276(19)	0.9461(21)

TABLE XXI. Fit results of the continuum extrapolation of  $K_{\ell 3}$  form factors at the physical point using monopole, quadratic, and z-parameter expansion fit forms, defined in Eqs. (A2)–(A7), together with the value of the uncorrelated  $\chi^2/\text{dof}$ .

	monopole	quadratic	z-parameter
$c_1^+$ [GeV $^{-2}$ ]	1.3108(69)	−1.275(10)	−2.058(17)
$c_1^0$ [GeV $^{-2}$ ]	0.868(30)	−0.835(32)	−1.335(49)
$c_2^+$ [GeV $^{-4}$ ]	...	1.615(96)	−0.24(23)
$c_2^0$ [GeV $^{-4}$ ]	...	0.809(89)	−0.69(16)
$\chi^2/\text{dof}$	0.32	0.28	0.31
$d_{21}^0$	1.01(26)	1.01(27)	1.39(37)
$e_{10}$ [GeV]	0.03032(81)	0.03033(81)	0.0300(88)
$e_{11}^+$ [GeV $^{-1}$ ]	0.2919(70)	0.2965(68)	0.2949(66)
$e_{11}^0$ [GeV $^{-1}$ ]	0.323(97)	0.32(10)	0.311(97)
$f_+(0)$	0.9614(10)	0.9614(10)	0.9616(10)
$\lambda_+^+$ [ $10^{-2}$ ]	2.554(14)	2.583(20)	2.567(21)
$\lambda_0^+$ [ $10^{-2}$ ]	1.691(59)	1.692(65)	1.665(60)
$\lambda_+''$ [ $10^{-3}$ ]	1.304(14)	1.275(76)	1.158(61)
$\lambda_0''$ [ $10^{-3}$ ]	0.572(40)	0.638(70)	0.591(55)

TABLE XXII. The same table as Table XIV, but for each fit result listed in Table XXI.

	monopole	quadratic	z-parameter
$I_{K^0}^e$	0.154744(83)	0.154781(75)	0.154710(77)
$I_{K^0}^\mu$	0.10320(15)	0.10322(16)	0.10313(16)
$I_{K^+}^e$	0.159118(85)	0.159155(77)	0.159519(80)
$I_{K^+}^\mu$	0.10621(16)	0.10623(17)	0.10653(17)
$f_+(0)\sqrt{I_{K^0}^e}$	0.37818(42)	0.37824(42)	0.37825(43)
$f_+(0)\sqrt{I_{K^0}^\mu}$	0.30885(44)	0.30889(45)	0.30883(45)
$f_+(0)\sqrt{I_{K^+}^e}$	0.38349(42)	0.38355(43)	0.38408(43)
$f_+(0)\sqrt{I_{K^+}^\mu}$	0.31331(45)	0.31335(46)	0.31387(46)

- 
- [1] P. A. Zyla *et al.* (Particle Data Group), PTEP **2020**, 083C01 (2020).
- [2] M. Moulson, PoS **CKM2016**, 033 (2017), arXiv:1704.04104 [hep-ex].
- [3] Y. Aoki *et al.*, (2021), arXiv:2111.09849 [hep-lat].
- [4] A. Bazavov *et al.* (Fermilab Lattice, MILC), Phys. Rev. **D87**, 073012 (2013), arXiv:1212.4993 [hep-lat].
- [5] P. A. Boyle, A. Jüttner, R. D. Kenway, C. T. Sachrajda, S. Sasaki, A. Soni, R. J. Tweedie, and J. M. Zanotti (RBC-UKQCD), Phys. Rev. Lett. **100**, 141601 (2008), arXiv:0710.5136 [hep-lat].
- [6] P. A. Boyle, J. M. Flynn, N. Garron, A. Jüttner, C. T. Sachrajda, K. Sivalingam, and J. M. Zanotti (RBC-UKQCD), JHEP **08**, 132 (2013), arXiv:1305.7217 [hep-lat].
- [7] P. A. Boyle *et al.* (RBC-UKQCD), JHEP **06**, 164 (2015), arXiv:1504.01692 [hep-lat].
- [8] S. Aoki, G. Cossu, X. Feng, H. Fukaya, S. Hashimoto, T. Kaneko, J. Noaki, and T. Onogi (JLQCD), Phys. Rev. **D96**, 034501 (2017), arXiv:1705.00884 [hep-lat].
- [9] A. Bazavov *et al.* (Fermilab Lattice, MILC), Phys. Rev. Lett. **112**, 112001 (2014), arXiv:1312.1228 [hep-ph].
- [10] N. Carrasco, P. Lami, V. Lubicz, L. Riggio, S. Simula, and C. Tarantino (ETM), Phys. Rev. **D93**, 114512 (2016), arXiv:1602.04113 [hep-lat].
- [11] A. Bazavov *et al.* (Fermilab Lattice, MILC), Phys. Rev. **D99**, 114509 (2019), arXiv:1809.02827 [hep-lat].
- [12] J. Kakazu, K.-i. Ishikawa, N. Ishizuka, Y. Kuramashi, Y. Nakamura, Y. Namekawa, Y. Taniguchi, N. Ukita, T. Yamazaki, and T. Yoshié (PACS), Phys. Rev. D **101**, 094504 (2020), arXiv:1912.13127 [hep-lat].
- [13] T. Yamazaki, K.-i. Ishikawa, N. Ishizuka, Y. Kuramashi, Y. Nakamura, Y. Namekawa, Y. Taniguchi, N. Ukita, and T. Yoshié (PACS), in *38th International Symposium on Lattice Field Theory* (2021) arXiv:2111.00744 [hep-lat].
- [14] C. Morningstar and M. J. Peardon, Phys. Rev. **D69**, 054501 (2004), arXiv:hep-lat/0311018 [hep-lat].
- [15] Y. Iwasaki, (2011), UTHEP-118, arXiv:1111.7054 [hep-lat].
- [16] E. Shintani and Y. Kuramashi (PACS), Phys. Rev. D **100**, 034517 (2019),

- arXiv:1902.00885 [hep-lat].
- [17] K. I. Ishikawa, N. Ishizuka, Y. Kuramashi, Y. Nakamura, Y. Namekawa, Y. Taniguchi, N. Ukita, T. Yamazaki, and T. Yoshié (PACS), Phys. Rev. **D99**, 014504 (2019), arXiv:1807.06237 [hep-lat].
- [18] P. A. Boyle, J. M. Flynn, A. Juttner, C. Kelly, H. P. de Lima, C. M. Maynard, C. T. Sachrajda, and J. M. Zanotti (RBC-UKQCD), JHEP **07**, 112 (2008), arXiv:0804.3971 [hep-lat].
- [19] S. Aoki, H. Fukaya, S. Hashimoto, J. Noaki, T. Kaneko, H. Matsufuru, T. Onogi, and N. Yamada (JLQCD), Phys. Rev. **D77**, 094503 (2008), arXiv:0801.4186 [hep-lat].
- [20] Y. Taniguchi, PoS **LATTICE2012**, 236 (2012), arXiv:1303.0104 [hep-lat].
- [21] J. Gasser and H. Leutwyler, Nucl. Phys. **B250**, 517 (1985).
- [22] J. Gasser and H. Leutwyler, Nucl. Phys. **B250**, 465 (1985).
- [23] C. Allton *et al.* (RBC-UKQCD), Phys. Rev. **D78**, 114509 (2008), arXiv:0804.0473 [hep-lat].
- [24] S. Aoki *et al.* (PACS-CS Collaboration), Phys. Rev. **D79**, 034503 (2009), arXiv:0807.1661 [hep-lat].
- [25] K. I. Ishikawa, N. Ishizuka, Y. Kuramashi, Y. Nakamura, Y. Namekawa, Y. Taniguchi, N. Ukita, T. Yamazaki, and T. Yoshie (PACS), PoS **LATTICE2015**, 075 (2016), arXiv:1511.09222 [hep-lat].
- [26] J. Kakazu, K.-I. Ishikawa, N. Ishizuka, Y. Kuramashi, Y. Nakamura, Y. Namekawa, Y. Taniguchi, N. Ukita, T. Yamazaki, and T. Yoshie (PACS), PoS **LATTICE2016**, 160 (2017).
- [27] A. Ali Khan *et al.* (CP-PACS), Phys. Rev. D **65**, 054505 (2002), [Erratum: Phys.Rev.D 67, 059901 (2003)], arXiv:hep-lat/0105015.
- [28] C. Bourrely, I. Caprini, and L. Lellouch, Phys. Rev. **D79**, 013008 (2009), [Erratum: Phys. Rev.D82,099902(2010)], arXiv:0807.2722 [hep-ph].
- [29] J. Bijnens and K. Ghorbani, (2007), arXiv:0711.0148 [hep-ph].
- [30] M. Di Carlo, D. Giusti, V. Lubicz, G. Martinelli, C. T. Sachrajda, F. Sanfilippo, S. Simula, and N. Tantalo, Phys. Rev. **D100**, 034514 (2019), arXiv:1904.08731 [hep-lat].
- [31] C. Dawson, T. Izubuchi, T. Kaneko, S. Sasaki, and A. Soni, Phys. Rev. **D74**, 114502 (2006), arXiv:hep-ph/0607162 [hep-ph].
- [32] V. Lubicz, F. Mescia, S. Simula, and C. Tarantino (ETM), Phys. Rev. **D80**, 111502 (2009), arXiv:0906.4728 [hep-lat].

- [33] V. Bernard, M. Oertel, E. Passemar, and J. Stern, Phys. Rev. **D80**, 034034 (2009), arXiv:0903.1654 [hep-ph].
- [34] M. Antonelli *et al.* (FlaviaNet Working Group on Kaon Decays), Eur. Phys. J. **C69**, 399 (2010), arXiv:1005.2323 [hep-ph].
- [35] H. Leutwyler and M. Roos, Z. Phys. **C25**, 91 (1984).
- [36] C.-Y. Seng, D. Galviz, W. J. Marciano, and U.-G. Meißner, Phys. Rev. D **105**, 013005 (2022), arXiv:2107.14708 [hep-ph].
- [37] C.-Y. Seng, M. Gorchtein, H. H. Patel, and M. J. Ramsey-Musolf, Phys. Rev. Lett. **121**, 241804 (2018), arXiv:1807.10197 [hep-ph].
- [38] J. C. Hardy and I. S. Towner, Phys. Rev. C **102**, 045501 (2020).
- [39] C.-Y. Seng, D. Galviz, M. Gorchtein, and U.-G. Meißner, (2022), arXiv:2203.05217 [hep-ph].
- [40] C.-Y. Seng, D. Galviz, M. Gorchtein, and U. G. Meißner, Phys. Lett. B **820**, 136522 (2021), arXiv:2103.00975 [hep-ph].
- [41] C.-Y. Seng, D. Galviz, M. Gorchtein, and U.-G. Meißner, JHEP **11**, 172 (2021), arXiv:2103.04843 [hep-ph].